



Published in final edited form as:

Nat Chem Biol. 2021 April ; 17(4): 465–476. doi:10.1038/s41589-020-00734-x.

Phospholipase iPLA₂β Averts Ferroptosis By Eliminating A Redox Lipid Death Signal

Wan-Yang Sun^{1,2,3}, Vladimir A. Tyurin¹, Karolina Mikulska-Ruminska^{4,5}, Indira H. Shrivastava^{1,5}, Tamil S. Anthonymuthu^{1,11}, Yu-Jia Zhai^{2,3}, Ming-Hai Pan^{2,3}, Hai-Biao Gong^{2,3}, Dan-Hua Lu^{2,3}, Jie Sun^{2,3}, Wen-Jun Duan^{2,3}, Sergey Korolev⁶, Andrey Y. Abramov⁷, Plamena R. Angelova⁷, Ian Miller⁶, Ofer Beharier¹⁰, Gao-Wei Mao¹, Haider H. Dar¹, Alexandr A. Kapralov¹, Andrew A. Amoscato¹, Teresa G. Hastings⁸, J. Timothy Greenamyre⁸, Charleen T. Chu⁹, Yoel Sadovsky¹⁰, Ivet Bahar⁵, Hülya Bayır^{1,11}, Yulia Y. Tyurina^{1,**}, Rong-Rong He^{2,3,**}, Valerian E. Kagan^{1,12,13,14,15,**}

¹Department of Environmental and Occupational Health and Center for Free Radical and Antioxidant Health, University of Pittsburgh, Pittsburgh, Pennsylvania 15260, USA ²Guangdong Engineering Research Center of Chinese Medicine & Disease Susceptibility, College of Pharmacy, Jinan University, Guangzhou, Guangdong 510632, China ³International Cooperative Laboratory of Traditional Chinese Medicine Modernization and Innovative Drug Development of Chinese Ministry of Education (MoE), College of Pharmacy, Jinan University, Guangzhou, Guangdong 510632, China ⁴Institute of Physics, Faculty of Physics, Astronomy and Informatics, Nicolaus Copernicus University in Toruń, Grudziadzka 5, 87-100 Toruń, Poland ⁵Department of Computational and Systems Biology, School of Medicine, University of Pittsburgh, Pennsylvania 15260, USA ⁶Edward A. Doisy Department of Biochemistry and Molecular Biology, Saint Louis University School of Medicine, St. Louis, Missouri 63104, USA ⁷UCL Queen Square Institute of Neurology, Department of Clinical and Movement Neurosciences, University College London, Queen Square, London WC1N 3BG, United Kingdom ⁸Department of Neurology, University of Pittsburgh, Pittsburgh, Pennsylvania 15213, USA ⁹Department of Pathology, University of Pittsburgh, Pittsburgh, Pennsylvania 15213, USA ¹⁰Magee Womens Research Institute and Department of OBGYN, University of Pittsburgh, Pittsburgh, Pennsylvania 15213, USA ¹¹Department of Critical Care Medicine, Safar Center for Resuscitation Research, Children's Neuroscience Institute, Children's Hospital of Pittsburgh, University of Pittsburgh, Pittsburgh, Pennsylvania 15260, USA ¹²Department of Radiation Oncology, University of Pittsburgh, Pittsburgh, Pennsylvania 15260, USA ¹³Department of Chemistry, University of Pittsburgh, Pittsburgh, Pennsylvania 15260, USA ¹⁴Department of Pharmacology and Chemical Biology,

Users may view, print, copy, and download text and data-mine the content in such documents, for the purposes of academic research, subject always to the full Conditions of use:http://www.nature.com/authors/editorial_policies/license.html#terms

**corresponding authors: kagan@pitt.edu; rongronghe@jnu.edu.cn; yyt1@pitt.edu.

AUTHOR CONTRIBUTIONS: VEK, R.-RH, HB, YYT and YS conceived the study. YJZ, OB, HHD and OK performed experiments with cells. SK and IM cloned and purified the WT and mutant iPLA₂β protein. VEK, HB, CTC, TGH, R.R.-H and W.-J.D. designed *in vivo* experiments; W.-Y.S., M.-H.P., D.-H.L., Y.-J.Z and JS performed *in vivo* experiments. VEK, YS, YYT, HB, AYA, PRA and R.-RH designed *in vitro* experiments; W.-Y.S. and VAT performed *in vitro* experiments. WYS, VAT, AAA, TA, and HBG performed MS measurements and analyzed data. W.-Y.S., YYT and VAT discussed and interpreted MS results. K.M.-R. and IHS performed computational modeling and analyzed data. IB supervised computational studies and interpreted the results. W.-Y.S., IB, YS, CC, IHS, BL and HB participated in writing the manuscript. YYT and VEK wrote the manuscript.

DECLARATION OF INTERESTS: The authors have declared that no conflict of interest exists.

University of Pittsburgh, Pittsburgh, Pennsylvania 15260, USA ¹⁵Institute of Regenerative Medicine, IM Sechenov Moscow State Medical University, Moscow 119048, Russia

Abstract

Ferroptosis, triggered by discoordination of iron, thiols and lipids, leads to accumulation of 15-hydroperoxy-arachidonoyl-PE (15-HpETE-PE) generated by complexes of 15-lipoxygenase (15-LOX) and a scaffold protein, PEBP1. As Ca²⁺-independent phospholipase PLA₂ (iPLA₂β, *PLA2G6/PNPLA9* gene), can preferentially hydrolyze peroxidized phospholipids, it may eliminate ferroptotic 15-HpETE-PE death signal. Here we demonstrate that by hydrolyzing 15-HpETE-PE, iPLA₂β averts ferroptosis whereas its genetic or pharmacological inactivation sensitizes cells to ferroptosis. Given that *PLA2G6/PNPLA9* mutations relate to neurodegeneration, we examined fibroblasts from a patient with a Parkinson's disease (PD)-associated mutation fPD^{R747W} and found selectively decreased 15-HpETE-PE hydrolyzing activity, 15-HpETE-PE accumulation and elevated sensitivity to ferroptosis. CRISPR-CAS9-engineered *PNPLA9*^{R748W/R748W} mice exhibited progressive parkinsonian motor deficits and 15-HpETE-PE accumulation. Elevated 15-HpETE-PE levels were also detected in midbrains of rotenone-infused parkinsonian rats and α-synuclein mutant SNCA-A53T mice with decreased iPLA₂β expression and PD-relevant phenotype. Thus, iPLA₂β is a new ferroptosis regulator and its mutations may be implicated in PD pathogenesis.

INTRODUCTION

The fidelity of biological systems depends on either re-programming or elimination of unnecessary or harmful cells and/or their organelles via several cell death programs¹. Ferroptosis is a type of regulated cell death² triggered by the discoordination of three major metabolic pillars – iron, lipids and thiols - culminating in lipid peroxidation³ The term “ferroptosis” reflects two specific roles of iron in: i) the production of membrane (phospho)lipid (PL) hydroperoxides and ii) “splitting” the weak hydroperoxy O-O bond⁴ to yield oxidatively-truncated electrophilic products, considered as the proximate executioners of ferroptotic death⁴. A seleno-peroxidase, glutathione peroxidase 4 (GPX4), reduces membrane phospholipid hydroperoxides to alcohols⁵, thus “neutralizing” the high-risk O-O-containing intermediates⁶.

Hydroperoxy-arachidonoyl-(C20:4, eicosatetraenoyl, ETE or AA)- and adrenoyl-(C22:4, docosa-tetraenoyl, DTE)-phosphatidylethanolamines (PE) (HpETE-PE and HpDTE-PE) have been identified as characteristic pro-ferroptotic signals² Accordingly, esterification of these two fatty acid residues into PE by ACSL4 and re-acylation of lyso-PE (LPE) by LPCAT3 are important ferroptosis regulators⁷. High selectivity and specificity of ETE-PE and DTE-PE oxidation at their 15th and 17th carbons, respectively, is a feature of ferroptotic lipid peroxidation⁸ suggesting the involvement of enzymatic catalysis⁸. Indeed, 15-lipoxygenase (15-LOX) complexed with a scaffold-protein, PE-binding protein 1 (PEBP1), has been identified as a generator of pro-ferroptotic 15-HpETE-PE and 17-HpDTE-PE⁹. One can assume that a phospholipase A₂ (PLA₂) capable of hydrolyzing *sn*-2-oxygenated

polyunsaturated fatty acid (PUFA)-PE residues would eliminate the ferroptotic signal whereas genetic or chemical ablation of this activity would be pro-ferroptotic. Ca^{2+} -independent iPLA₂β (PNPLA9 from *PLA2G6* family) can hydrolyze oxidized phospholipids¹⁰, yet its catalytic competence towards ferroptotic signals has not been hitherto tested.

Ferroptosis has been implicated in a number of diseases, including Parkinson's disease (PD)¹¹. Death of dopaminergic neurons in the *substantia nigra pars compacta* is one of the hallmarks of PD¹¹. Enhanced oxidative stress and lipid peroxidation caused by the mishandling of iron and dopamine oxidation are important causative factors, along with the dysregulation of autophagy which otherwise regulates ferroptosis by degrading iron storage proteins¹². Based on the striking similarity of the PD pathogenesis and pro-ferroptotic factors, it has been suggested that ferroptosis is involved in PD pathogenesis¹¹. *PNPLA9* mutations have been associated with several iPLA₂β-related neurodegenerative diseases (PLAN). Based on the age of onset and progressive clinical features, several PLAN subtypes have been identified: infantile neuroaxonal dystrophy (INAD), atypical neuroaxonal dystrophy (ANAD) and a Parkinsonian syndrome with adult onset dystonia and autosomal recessive early-onset Parkinsonism¹³. Thus, we tested a hypothesis that deficiency in iPLA₂β caused by genetic or pharmacological perturbations preserves the death signal, 15-HpETE-PE, hence propagates ferroptosis. Here we demonstrated that genetic abatement of iPLA₂β in SH-SY5Y neuronal cells, H109 fibroblasts, and BeWo trophoblasts, or a naturally occurring mutation in the *PNPLA9* gene encoding for iPLA₂β (*R747W*) in fibroblasts from a dystonic PD patient (fPD^{*R747W*} cells) result in: i) lowered hydrolytic activity towards 15-HpETE-PE, ii) elevated intracellular contents of 15-HpETE-PE, and iii) enhanced sensitivity to ferroptosis vs. WT controls. We documented that CRISPR-engineered *Pnpla9^{R748W/R748W}* mice exhibit progressive Parkinsonian motor deficits along with 15-HpETE-PE accumulation. We detected decreased iPLA₂β activity and elevated 15-HpETE-PE levels in the midbrains of rotenone-infused parkinsonian rats as well as 8-month-old SNCA-A53T mutant mice with decreased iPLA₂β expression and PD-relevant phenotype¹⁴. These data along with computational modeling permitted us to decipher and predict the impact of impairments of iPLA₂β and its *R747W* mutant on ferroptotic death relevant to PD pathogenesis.

RESULTS

15-HpETE-PE is a preferred substrate of iPLA₂β.

To assess iPLA₂β hydrolytic activity (Fig. 1a), we biosynthesized 1-SA-2-15-HpETE-PE and purified it to ~99% homogeneity (as evidenced by LC-MS analysis (Supplementary Fig. 1a)). We also expressed, isolated and purified recombinant iPLA₂β¹⁵ (Extended Data Fig. 1a) and tested its activity by LC-MS of the products: lyso-PE (1-SA-2-OH-PE) (Fig. 1a,b) and fatty acids (ETE or 15-HpETE) (Extended Data Fig. 1b,c). While both substrates (1-stearoyl-2-eicosatetraenoyl-phosphatidylethanolamine (1-SA-2-ETE-PE) and 1-stearoyl-2-15-hydroperoxy-eicosatetraenoyl-phosphatidylethanolamine (1-SA-2-15-HpETE-PE)) were readily hydrolyzed by the enzyme, the activity towards 1-SA-2-15-HpETE-PE was markedly higher than towards non-oxidized PE (Fig. 1a). Based on the kinetic

SA-2-15-HpETE-PE (Fig. 2a,b). Quantitative analysis (Extended Data Fig. 7a,b) showed that select residues (e.g. K566PLP568 and H517 in monomer A and R656-P657, W661, T650, K665 and F668 in monomer B) had the strongest interactions with 1-SA-2-15-HpETE-PE.

R747W mutation reduces iPLA₂β activity with 15-HpETE-PE.

Several mutations in the catalytic domain (CAT) of the *PNPLA9* gene have been associated¹⁵ with neuropathies and PD¹⁹. We found that the activity of one of the mutant proteins (*R747W*, or *R693W* in the short variant) displayed a slightly lower activity towards non-oxidized ETE-PE and a markedly greater loss of activity towards 15-HpETE-PE (Fig. 1a). We next assessed the endogenous phospholipase activity in control and fPD^{*R747W*} cells using two protocols to directly measure the hydrolytic potency of iPLA₂β towards non-oxygenated substrates and 15-HpETE-PE. To distinguish between general PLA₂ activity and specific iPLA₂β activity, we employed an inhibitor, (*S*)-bromo-enol lactone ((*S*)-BEL), a chiral-specific suicidal substrate that discriminates iPLA₂β from all other phospholipases²⁰ (Extended Data Fig. 8a). General PLA₂ activity was slightly (1.3-fold) but significantly lower in fPD^{*R747W*} cells than in control cells (Fig. 1g, *left*). The activity towards exogenously added 1-SA-2-15-HpETE-PE was sharply lower (>5-fold) in fPD^{*R747W*} cells vs control cells (Fig. 1g, *right*). Western blotting (Fig. 1h) showed no differences in iPLA₂β content between control and fPD^{*R747W*} cells. Thus, *R747W* mutation specifically suppressed catalytic competence towards 15-HpETE-PE.

To explore the molecular basis of the lowered catalytic potency of *PNPLA9* mutant *R747W* towards 1-SA-2-15-HpETE-PE, we repeated our simulations with the mutant dimer. The simulations showed that *R747W* mutation affected the interfacial packing between the two CAT domains of the dimer resulting in two effects: i) the catalytic site became less accessible, and ii) the association of the mutant with the membrane weakened (Fig. 2a,b). This supports the experimentally observed lower hydrolytic activity of the *R747W* mutant toward 1-SA-2-15-HpETE-PE.

Ferroptosis in fPD^{*R747W*} and iPLA₂β-deficient cells.

Next we determined the content of phospholipids and phospholipid oxidation products in WT H109 and fPD^{*R747W*} cells after triggering ferroptosis by a GPX4 inhibitor, RSL3. Using global phospholipidomics we found that phospholipid compositions of H109 cells and fPD^{*R747W*} fibroblasts were very similar and included 86 species of PE, 78 species of PC, 28 species of PI and 32 species of PS (Fig. 3a and Extended Data Fig. 8b). PE included diacyl- (55.2±0.8 and 56.9±0.6% of total PE) and alkenyl- (44.8±0.8 and 43.1±0.6% of total PE) molecular species in H109 cells and fPD^{*R747W*} cells, respectively. The contents of diacyl-PE species containing arachidonic, adrenic and docosahexaenoic acid in H109 and fPD^{*R747W*} cells were 17.2±0.2, 7.4±0.1, 0.8±0.1% of total PE species and 15.9±0.1, 9.6±0.1 and 1.0±1.1% of total PE, respectively. No significant differences in the contents of alkenyl-PE species were detected: 24.4±0.5, 8.4±0.2, 1.9±0.1% of total PE species and 20.8±0.3, 10.3±0.2 and 2.0±0.1% for arachidonoyl, adrenoyl and docosahexanoyl-PE species, respectively. PC class contained mostly diacyl molecular species, 96.0±0.1% of total PC. The species containing arachidonic acid (36:4; 38:4 and 38:5) were predominant. The major

arachidonoyl-PI species, 38:4, was accountable for 47.4±0.3 and 46.4±0.5 % of total PI in H109 and fPD^{R747W} cells, respectively. PUFA-containing PS species were mainly represented by species with arachidonic (38:4) and adrenic acid (40:4).

Redox phospholipidomics revealed increased levels of a variety of mono-, di- and tri-oxygenated species of PE, PC, PS and PI species in fPD^{R747W} vs H109 cells triggered to undergo ferroptosis by a GPX4 inhibitor, RSL3 (Fig. 3b,c and Extended Data Fig. 8c). An unbiased OPLS-DA analysis established that oxidized PE (PEox) species were the predominant oxidized phospholipids accumulating in WT H109 and fPD^{R747W} mutant cells upon RSL3 treatment (Fig. 3d,e). Notably, RSL3 treated fPD^{R747W} cells contained greater amounts of oxidized PE species (Extended Data Fig. 8c) and exhibited significantly higher levels of pro-ferroptotic 15-HpETE-PE both basally and after RSL3 treatment (Fig. 3c). 15-HpETE-PE level was 2.4-fold higher after RSL3 treatment in fPD^{R747W} cells than in WT cells (Fig. 3c). Two of the major PC-ox species were lower in fPD^{R747W} cells compared to H109 cells (Fig. 3d,e).

We asked if the human PD-associated *R747W* mutation in *PNPLA9* increases the sensitivity of fPD^{R747W} cells to pro-ferroptotic stimulation. The time-course and concentration-dependence of cell death triggered by RSL3 (Fig. 4a) showed a higher sensitivity to ferroptosis of fPD^{R747W} cells, both in terms of the lower RSL3 concentration required for the ferroptotic response and its earlier onset in the fPD^{R747W} cells. The specificity of RSL3-induced ferroptotic death was confirmed by negative responses to inhibitors of alternative death programs – apoptosis (z-VAD-fmk) and necroptosis (necrostatin-1s) (Fig. 4b), whereas four inhibitors of ferroptosis (Fer-1, DFO, Vitamin E, Baicalein) inhibited RSL3-induced cell death.

To explore whether the anti-ferroptotic potential of iPLA₂β is realized in other cell types, we compared the sensitivity to ferroptosis in WT and several iPLA₂β KD cells: H109 fibroblasts, SH-SY5Y neuronal cells and BeWo trophoblasts. A markedly enhanced sensitivity of iPLA₂β-deficient cells to RSL3 induced ferroptosis vs WT controls was found (Fig. 4c and Extended Data Fig. 8d,e). Moreover, iPLA₂β-deficient cells exhibited higher levels of pro-ferroptotic PE biomarkers detected by LC-MS (Extended Data Fig. 8f).

To demonstrate the role of remodeling of membrane phospholipids we knocked-down LPCAT3 in WT H109 cells (human fibroblasts) and mouse embryonic fibroblasts (MEF) and characterized the deacylation/reacylation processes by LC-MS. The levels of LPCAT3 expression assessed by western blotting decreased 2- and 1.5-fold in H109 and MEF cells, respectively (Fig. 4d and Extended Data Fig. 9a). This was accompanied by the increased resistance to ferroptosis by 50% and 60% (Fig. 4e and Extended Data Fig. 9b). Expectedly, LPCAT3 KD resulted in increased levels of the hydrolyzed arachidonoyl-PL metabolites, lyso-PE (1-SA-2-OH-PE) and lyso-PC (1-SA-2-OH-PC) (Fig. 4f and Extended Data Fig. 9c). In both cell lines the levels of the major pro-ferroptotic signal, peroxidized ETE-PE (1-SA-2-HpETE-PE) was increased upon exposure to RSL3; its content in LPCAT3 KD cells treated with RSL3 was significantly lower (Fig. 4g and Extended Data Fig. 9d). Human and mouse fibroblasts generated oxygenated arachidonoyl-PC in response to RSL3 treatment. Similarly, in RSL3-treated LPCAT3 KD cells, the level of 1-SA-2-HpETE-PC was lower vs

RSL3 treated controls (Fig. 4g and Extended Data Fig. 9d). Analogous results were obtained for adrenoyl-PE and adrenoyl-PC species (Supplementary Fig. 2). RSL3 induced accumulation of PL-OOH, disorganized the membrane and facilitated the hydrolysis of both oxidatively modified PLs and non-oxidized PLs. Consequently, the amounts of lyso-PLs were higher than that of PL-OOH. These results support the LPCAT3 involvement in ferroptosis regulation via remodeling of membrane phospholipids (Lands cycle) and maintaining high AA-PE levels required for the generation of pro-ferroptotic death signals.

Parkinsonian phenotype of homozygous *Pnpla9*^{R747W} mice.

Assuming that human *PNPLA9*^{R747W} mutation and the compromised control of pro-ferroptotic PE-derived signals may cause enhanced death of dopaminergic neurons, we employed by CRISPR/Cas genome editing, and created a mouse with an R748W point mutation at the mouse *Pnpla9* locus, corresponding to R747W of human *PNPLA9* (Supplementary Fig. 3. and 4a–c). In the homozygous *Pnpla9*^{R748W/R748W} mice, we observed motor impairments (Fig. 5a–c and Supplementary Fig. 4d,e) documented using the pole test (Fig. 5a and Movie 4) and rotarod test (Fig. 5b and Movie 5) which started at 3–4 months. Quantitative catwalk tests indicated that *Pnpla9*^{R748W/R748W} mice had reduced average walking speed, increased walking speed variation, and disrupted walking cycle, when compared with WT and *Pnpla9*^{WT/R748W} mice (Fig. 5c). Motor impairments were not detected in heterozygous *Pnpla9*^{WT/R748W} mice, confirming the human data that only homozygous mutants develop behavioral deficiencies related to PD pathogenesis²¹, which is consistent with its role in causing autosomal recessive PD.

In homozygous *Pnpla9*^{R748W/R748W} mutant mice, the midbrain levels of tyrosine hydroxylase (TH), a marker for dopaminergic neurons, were significantly decreased (Fig. 5d), indicating a more than 40% reduction of dopaminergic neurons. Consistently, dopamine (DA) - the product of TH - and its primary metabolites 3,4-dihydroxyphenylacetaldehyde (DOPAL) and 3-methoxytyramine (3-MT) in the striatum of mutant mice were also significantly decreased (Fig. 5e). We also observed elevated levels of a characteristic peroxidation product, 4-hydroxynonenal, 4-HNE (Fig. 5f), and lower contents of intracellular antioxidant glutathione, GSH (Fig. 5g) in the mutant mouse midbrain. Monomeric α -synuclein and α -synuclein aggregates did not accumulate in the mutant mice (Supplementary Fig. 4f,g).

PEox in midbrain of homozygous *Pnpla9*^{R748W} mice.

Redox phospholipidomics of midbrain samples revealed elevated levels of 15-HpETE-PE in *Pnpla9*^{R748W/R748W} vs. WT mice (Fig. 5h). Assessment of the specific hydrolytic competency towards 15-HpETE-PE showed that the activity was sharply decreased (more than 75%) in the brain homogenates of *PNPLA9* mutant vs WT mice (Fig. 5i and Supplementary Fig. 4h). Western blotting showed no differences in the iPLA₂ β protein contents between the two groups of mice (Fig. 5j).

PNPLA9 mutations have been linked to the pathogenesis of several neurodegenerative diseases¹⁹, including PD. To comparatively evaluate the effect of the R747W mutation on iPLA₂ β function and the pathogenicity potential vs all possible mutations we performed *in*

silico saturation mutagenesis analysis using a machine learning tool Rhapsody²² (Supplementary Fig. 5). This analysis confirmed a highly deleterious nature and high pathogenicity score of the *R747W*.

PEox in midbrains of rotenone infused rats.

By using phospho-lipidomics analysis in another PD model, rotenone infused rats, we identified 74 species of PE, 67 species of PC, 22 species of PI and 31 species of PS (Fig. 6a, Extended Data Fig. 10a and Supplementary Fig. 6a). The level of the PE plasmalogens was 1.9 times higher than that of diacyl-PEs. The contents of PE with arachidonic, adrenic and docosahexaenoic residues were 4.5 ± 0.5 , 7.1 ± 0.3 , $8.9\pm 1.4\%$ (of total PE) for diacyl species and 7.2 ± 0.7 , 1.0 ± 0.1 and $11.4\pm 1.2\%$ for alkenyl PE species. In the PC class, diacyl-species were the most abundant and their content was 15.2 times higher vs. alkenyl-PC. The contents of arachidonoyl- and docosahexaenoyl species were 7.1 ± 0.5 and 6.8 ± 0.3 vs. 0.13 ± 0.01 and 0.03 ± 0.01 (% of total PC) for diacyl- and alkenyl PCs, respectively. The PS class included high amounts of arachidonic (38:4) and docosahexaenoic acid (40:6) species: 10.0 ± 0.8 and 24.7 ± 3.3 % (of total PS). Among PIs, the arachidonoyl species (38:4) was predominant - 62.7 ± 1.6 %. No significant differences in the molecular speciation of major phospholipids and their relative contents were found between WT and Parkinsonian rats. Redox lipidomics revealed significantly elevated levels of pro-ferroptotic 15-HpETE-PE and 17-HpDTE-PE in midbrain tissue on days 10–14 after rotenone infusion (Fig. 6b,c and Extended Data Fig. 10b), when the characteristic manifestations of PD-related syndrome are clearly detectable²³. Furthermore, the contents of PE species containing oxo-arachidonoyl-residues (1-SA-2-oxo-ETE-PE, 1-SA-2-oxo-hydroperoxy-ETE-PE as well as 1-SA-2-hydroxy-ETE-PE) were significantly increased in Parkinsonian rats vs control rats (Supplementary Fig. 6b). Direct assessments of the 15-HpETE-PE-hydrolyzing activity revealed significantly lower rates in rotenone-treated brain homogenates vs non-treated controls (Fig. 6d).

PEox in midbrains of A53T transgenic mice.

The SNCA-A53T mutation is associated with autosomal dominant PD and elicits a PD disease-relevant phenotype in rodents¹⁴. A53T α Syn can indirectly – via suppression of mitogen-activated protein kinase (MAPK) signaling – negatively regulate the expression of PNPLA9²⁴. Indeed, western blotting of iPLA₂ β revealed significantly decreased expression levels of the protein in the midbrain of 8-month-old SNCA-A53T mutant mice vs WT mice (Extended Data Fig. 10c). In transgenic mice overexpressing human α -synuclein (α Syn) with A53T mutation, redox lipidomics revealed higher levels of oxygenated PEs in midbrains (Extended Data Fig. 10d) including the species that were identified as ferroptotic cell death signals (Extended Data Fig. 10e). PUFA-PE containing arachidonic and docosahexaenoic acid were predominant species. No differences in the molecular speciation and contents of PE between midbrains of WT and A53T mice (Extended Data Fig. 10f) were detected.

DISCUSSION

Necro-inflammatory consequences of ferroptosis and its possible pathogenic role in major acute and chronic degenerative diseases stimulated studies of its regulation. Identification of enzymatic lipid regulating mechanisms of ferroptosis, - ACSL4, LPCAT3²⁵, along with 15-HpETE-PE generation by 15LOX/PEBP1 complexes⁹ - was followed by the discoveries of new regulatory cascades including FSP1^{26, 27} and iNOS⁶. Here we demonstrate that iPLA₂β-can act as an anti-ferroptotic guardian via elimination of the pro-ferroptotic signal, 15-HpETE-PE. The peroxidized acyl chain of 15-HpETE-PE is exposed to the membrane surface (the whisker model¹⁶), thus enabling interfacial interaction with membrane-bound catalytic domains of the dimeric iPLA₂β. This alternative 15-HpETE-PE neutralizing mechanism may act in coordination with the reductive GPX4-dependent pathway or independently of it, serving as an additional check-point for preventing unnecessary or excessive ferroptotic death. The role of this pathway may be particularly important when the thiol-driven defenses become insufficient. Consequently, failure or deficiency in iPLA₂β - caused by genetic factors or chemical/pharmacological poisoning - may be associated with increased sensitivity to ferroptotic death.

Replenishment of oxidatively modified phospholipids may occur via the Kennedy and the Lands pathways whereby the latter involves, as the first step, deacylation to produce lysophospholipids followed by their reacylation²⁸. The deacylation step is the function of PLA₂, and the reacylation is mediated by lysophospholipid acyltransferase. In ferroptosis, of particular importance is the elimination of the unstable primary molecular products of lipid peroxidation, PL-OOH. This can be achieved through either direct reduction of hydroperoxy-group by GPX4/GSH system or hydrolysis of HOO-PUFA-phospholipids and subsequent reduction of the HOO-PUFA (eg, by non-heme peroxidases). As pro-ferroptotic peroxidation specifically targets arachidonoyl-containing PE species, this defines the specificity of ferroptotic phospholipid-metabolizing machinery. Both acyl-CoA synthetase long-chain family member 4 (ACSL4) and LPCAT3 display selectivity towards arachidonoyl-specific reactions²⁵. Vectorial uptake of exogenous fatty acids by fatty acid transport proteins (FATPs) coupled with their activation to CoA-thioesters can participate in the metabolism of peroxidized phospholipids. FATP2, one of the six members of the FATP family, displays specificity for arachidonic (C20:4) and adrenic (C22:4) fatty acids²⁹ pointing to its potential role in ferroptosis

Ca²⁺-independent PLA₂s (iPLA₂, group VI) are involved in the remodeling of membranes facilitated by the hydrolysis of oxidatively-modified PUFA-phospholipids followed by their re-acylation. The iPLA₂β preference towards hydrolyzing arachidonoyl-substrates³⁰ supports its anti-ferroptotic role in eliminating peroxidized arachidonoyl-PE species. Several studies in liposomes, isolated cell membranes and tissue homogenates support this role of iPLA₂ in the “repair” of peroxidized phospholipids^{10, 31}. As a member of the iPLA₂ family, iPLA₂β protects different cells from oxidative injury. Overexpression of iPLA₂β in INS-1 insulinoma cells enhanced repair of oxidized mitochondrial cardiolipins (CL) and protected against mitochondria-driven prooxidant cell death³². In the retina, an inhibitor of iPLA₂, bromophenol lactone (BEL), stimulated the accumulation of Fe-induced lipid peroxidation products³³. Elevated Fe levels, oxidative stress and lipid peroxidation have been implicated

in retinal damage in age-related macular degeneration (AMD)³⁴. Given the selectivity of iPLA₂β towards *sn*-2-arachidonoyl phospholipids, including PE³⁰, one can assume that the enzyme deficiency may be a part of the pro-ferroptotic mechanism in the retina relevant to the AMD pathogenesis.

Metabolic features of dopaminergic neurons with their high abundance of iron required for dopamine biosynthesis and high levels of redox-active intermediates of dopamine oxidation create pro-oxidant microenvironments¹¹. Among the most common manifestations of this are GSH deficiency, suppressed activity of GPX4¹², and elevated levels of lipid peroxidation products³⁵ - all typical characteristics of cells primed to ferroptotic death². Not surprisingly, the possible engagement of ferroptotic death in PD pathogenesis has been widely discussed, yet specific mechanisms for triggering ferroptosis in PD dopaminergic neurons remained enigmatic¹¹. The present study demonstrates that a typical PD-associated mutation in iPLA₂β results in a specific loss of catalytic activity towards one of the peroxidized PLs, the ferroptotic 15-HpETE-PE, in several cell culture and *in vivo* models. Interestingly, earlier work found no changes in the catalytic activity of iPLA₂β mutants associated with idiopathic PD³⁶. However these assessments did not examine oxygenated phospholipids, particularly 15-HpETE-PE, as substrates of the hydrolytic activity.

Our work demonstrates that, in addition to direct effects on iPLA₂β activity/expression, indirect regulatory factors altering iPLA₂β levels in critical cells/tissues may affect the ferroptotic signaling via 15HpETE-PE. We found that iPLA₂β expression was significantly reduced in a genetic model of rodent PD overexpressing the mutant A53T α.Syn. Both WT and A53T α.Syn suppressed MAPK signaling that regulates PNPLA9 expression²⁴. This could be attributed to the direct interaction of α.Syn with MAPKs such as ERK2 and its substrate ELK1, a transcription factor that binds the promoter of *Pnpla9*³⁷. We demonstrated that the decreased expression of iPLA₂β leads to a dampened pro-ferroptotic arachidonoyl-PE metabolism. Interestingly, a recent study in *Drosophila* showed that the loss of iPLA₂β leads to the shortening of phospholipid acyl chains, facilitating α.Syn aggregation³⁸. Thus, a vicious cycle involving α.Syn overexpression and iPLA₂β underexpression may be warranted.

Several Ca²⁺-independent phospholipases that belong to Group VI PLA(2) exhibit triacylglycerol (TAG) hydrolase activity³⁹. In the context of A53T mutation in SNCA, lower levels of iPLA₂β activity may be associated with the TAG accumulation in dopaminergic neurons. An increased fatty acid synthase expression and activation of Acyl-CoA synthetase⁴⁰ in SNCA A53Tmutants may lead to higher levels of free fatty acids, production of their CoA-derivatives and activation of esterification leading to the accumulation of TAGs. While TAG accumulation has been reported in ferroptosis⁴¹, mechanistically their role in the execution of this death program has not been clearly defined. It can be speculated that the hydrolytic activity of iPLA₂β towards TAGs may be viewed as a non-productive iPLA₂β distraction from its participation in hydrolysis of pro-ferroptotic peroxidized PE species, leading to an indirect enhancement of ferroptosis.

Taken together, our experimental results and the *in silico* studies strongly suggest that ineffective control/destruction of pro-ferroptotic signals as a consequence of PD-related

direct (*PNPLA9*), or indirect mutations leading to the reduced enzymatic hydrolytic activity of iPLA₂β following pesticide or other environmental exposures, may contribute to PD pathogenesis.

Online METHODS

Materials.

1-Octadecanoyl-2-(5*Z*,8*Z*,11*Z*,14*Z*-eicosatetraenoyl)-*sn*-glycero-3-phosphatidylethanolamine (1-SA-2-ETE-PE) was from Avanti Polar Lipids. 5*Z*,8*Z*,11*Z*,14*Z*-Eicosatetraenoic acid (ETE) and 15(*S*)-hydroxy-5*Z*,8*Z*,11*Z*,13*E*-eicosatetraenoic acid (15-HETE) was from Cayman Chemicals. Initially 15(*S*)-hydroperoxy-5*Z*,8*Z*,11*Z*,13*E*-eicosatetraenoic acid (15-HpETE) and 15(*S*)-hydroxy-5*Z*,8*Z*,11*Z*,13*E*-eicosatetraenoic acid (15-HETE) were synthesized and purified in our lab and later both 1-SA-2-15-HpETE-PE and 1-SA-2-15-HETE-PE became commercially available and were purchased from Cayman Chemicals. Unless otherwise stated, all other reagents were HPLC grade and purchased from ThermoFisher Scientific.

Animal models.

The experiments were approved by the Institutional Animal Care and Use Committee at the University of Pittsburgh (rat rotenone model) and the Laboratory Animal Ethics Committee at Jinan University (A53T overexpression and *PNPLA9*^{R748W} mouse models). Animal care and handling were in accord with National Institutes of Health guidelines.

Rat rotenone model: Rats were randomized in each study, and in all cases the surgeon and researchers evaluating the outcomes were blinded to the treatment group. Adult (7–9 months old, Charles River) male Lewis rats were subjected to a rotenone-induced model of PD as previously described⁴². Briefly, rats were injected intraperitoneally with vehicle or 3.0 mg/kg/day of rotenone (Sigma-Aldrich) either for one injection, five daily injections, or treated to Parkinsonian endpoint. Animals treated with rotenone to Parkinsonian endpoint (10–14 days) were sacrificed when animals displayed behavioral features including bradykinesia, postural instability/gait disturbances, and rigidity. Rat brains were removed from the skull, rinsed in cold 1×phosphate-buffered saline, placed on a cold Petri dish and cut in half into the right and left hemisphere. Using a blade and forceps precise microdissection of the ventral midbrain was performed and the tissue was flash frozen in liquid nitrogen and stored at 80°C.

A53T overexpression mouse model: Hα-Syn (A53T) transgenic C57BL/6J mice were from The Jackson Laboratory (Stock No: 006823) and bred. Animals were sacrificed at eight-months of age.

***Pnpla9*^{R748W} mouse model:** CRISPR/Cas-mediated genome engineering was used to create a C57BL/6N mouse model with point mutation (R748W) at *Pnpla9* locus. Briefly, the gRNAs to mouse *Pnpla9* gene, the donor oligo containing R748W (CGG to TGG) mutation, and Cas9 were co-injected into fertilized mouse eggs to generate targeted knockin offspring. Two silent mutations (GCC to GCG at A749) and (GGC to GGG at G755) were introduced

to prevent the binding and re-cutting of the sequence by gRNA after homology-directed repair. F0 founder animals were identified by PCR followed by sequence analysis, which were bred to wild-type mice to test germline transmission and F1 animal generation. The homozygous mutant mice were further generated by inter-cross heterozygous mutant mice. The gRNA target sequences are as follows: gRNA1 (F1, matching reverse strand of gene): GATGCCGACCATCTCGCACCAGG; gRNA2 (R1, matching forward strand of gene): CTGTGGATCGGGCCCCGGCCTGG. Animals were sacrificed at seven-months-old.

Cell lines.

H109 and fPD^{R747W} human primary fibroblasts obtained from a healthy and a R747W *PNPLA9* dystonia Parkinsonism patients⁴³ and mouse embryonic fibroblasts (ATCC, CRL-2991) were cultured in Dulbecco's modified Eagle's medium (ATCC); SH-SY5Y cells (ATCC, CRL-2266) were cultured in 1:1 mixture of Eagle's Minimum Essential Medium and F-12K Medium and BeWo human trophoblast cells (ATCC, CCL-98) were cultured in F-12K medium. All media were supplemented with 10% fetal bovine serum (Sigma-Aldrich) and 1% penicillin-streptomycin (ThermoFisher Scientific) and cells were at 37°C, 5% CO₂, and 95% humidity.

iPLA₂β knock-down.

Lentivirus vectors encoding sh*PNPLA9* (GCTGACGCCCTAGTGAATTC) were used to knockdown iPLA₂β in H109 and SH-SY5Y cells according to the manufacturer's instructions (Integrated Biotech Solutions Co., Ltd.). The pGMLV-SC5 lentiviral vector system containing sh*PNPLA9* was transformed into DH5α cells and the plasmid DNA was extracted and sequenced. For transfection, the plasmid was diluted with serum-free OMEM (Gibco) and incubated with Lipofectamine 3000 (ThermoFisher Scientific) before adding to cells for 6 hrs. After replacing the media, cells were cultured for 40 hrs. Transfection efficiency was optimized using a range of plasmid and Lipofectamine 3000 concentrations.

***PNPLA9* knockout in BeWo cells.**—BeWo cells that stably express the doxycycline-inducible Cas9 plasmid (Addgene plasmid #50661) were used for knocking out *PNPLA9*. Guide RNAs were designed using the CRISPR design tool (MIT), and expressed from pLKO5.sgRNA.EFS.tRFP657 (Addgene plasmid #57824) lentiviral system, initially in HEK293 cells, with virus used to infect BeWo cells (Guererro and Y Sadovsky, in submission).

***LPCAT3* knock-down (KD) in H109 and MEF cells.**—Cells were transfected with a mix of two Dicer substrate siRNAs (DsiRNA) against *LPCAT3* (hs.Ri.LPCAT3.13.1; 5' - CUUGGAACUGUAUUAGAUAAAUAUCA -3'; 3' - UGGAACCUUGACAUAUAUCUAUUUUAGU -5'; and hs.Ri.LPCAT3.13.2; 5' - CCAGUUCUCAUAUGAAUCACUACATG-3'; 3' - GGGGUCAAGAGUUACUUAGUGAUGUAC-5') for H109 WT and (mm.Ri.LPCAT3.13.1; 5' - GUCUUGACACUGAAGCUAAUUGGGC-3', 3' - CACAGAACUGUGACUUCGAUUAACCCG-5 and mm.Ri.LPCAT3.13.2; 5' - GUUUCUCUUCUGCCAAUCUACUACG-3'; 3' - AACAAAGAGAAGACG GUUAGAUGAUGC -5') for MEF or with control DsiRNA (51-01-14-04) using

Lipofectamine 3000 (Life technology) for 24 hrs, then counted and reseeded for experiments. Both si-NT or si-LPCAT3 cells (H109 and MEF) were treated with RSL3 after 48 hrs of transfection, and incubated for 20 hrs.

Ferroptosis assay.

H109 and fPD^{R747W} cells were treated with RSL3 (25nM) for 14 hrs in the absence or in the presence of ferrostatin-1 (Fer-1, 0.4 μ M) or z-VAD-fmk (50 μ M) or necrostatin-1s (20 μ M), or deferoxamine (10 μ M), or vitamin E (10 μ M), or baicalein (2 μ M). For SH-SY5Y WT and iPLA₂ β knockdown cells and BeWo WT and *PNPLA9* KO cells, RSL3 (2 μ M) or (100nM) was used for 18 hrs or 12 hrs with or without Fer-1 (0.4 μ M). Cell death was detected by LDH release using the CytoTox-ONE™ Cyto-toxicity Detection Kit (Promega).

iPLA₂ β cloning, expression, and purification.

Short variant CHO iPLA₂ β was cloned and expressed as described previously¹⁵. The short variant lacks a 54 amino acid (396–450) insert between ankyrin repeats and catalytic domain. The numbering is adjusted accordingly, such that R747W in Human Long iPLA₂ β is R693W in the CHO construct. CHO and human proteins have 90.4% sequence identity. Briefly, the *PNPLA9* gene cloned from CHO cells with a C-terminal 6XHisTag was cloned into pFastBac vector. CHO R693W mutant was obtained via Quikchange mutagenesis and was confirmed by complete sequencing (Source BioScience). The CHO iPLA₂ β protein was expressed in Sf9 cells (Invitrogen) and purified in purification buffer containing 25mM HEPES pH-7.5, 20% glycerol, 0.5M NaCl, 1mM TCEP on TALON cobalt resin (Clontech). iPLA₂ β and its mutant (R693W) were >95% pure as determined by Coomassie stained SDS-PAGE. Activity of purified proteins was confirmed using fluorescent phospholipase activity assay with Pyrene-PC (ThermoFisher Scientific #H361).

Assessment of iPLA₂ β activity.

Model system: 1-SA-2-ETE-PE (10 μ M) or 1-SA-2-15-HpETE (10 μ M) were incubated in 50mM PBS pH-7.4, containing 100 μ M DTPA in the presence of either WT iPLA₂ β or R747W mutant iPLA₂ β at 37°C. Both PEs were added as methanol solutions. Reaction was started by the addition of the enzyme (0.12 μ M). At different time points, lipids were extracted² and enzymatic activity was assessed by the formation of the hydrolysis products – 1-SA-2-OH-PE, ETE and 15-HpETE using LC/MS. To estimate the specificity constants, WT iPLA₂ β or R747W mutant iPLA₂ β were incubated in 50mM PBS (pH 7.4) containing DTPA (100 μ M) in the presence of different concentrations of 1-SA-2-ETE-PE (5–100 μ M) or 1-SA-2-15-HpETE-PE (5–150 μ M) or 1-SA-2-15-HETE-PE (50–100 μ M) for 5 min at 37°C. The reaction was stopped by the addition of chloroform:methanol (2:1, v/v). Hydrolysis product –1-SA-2-OH-PE - was extracted and resolved by LC/MS.

iPLA₂ β activity in cells and tissues.

Cells (1 \times 10⁶) were harvested after treatment with trypsin-EDTA (0.25%; Gibco), washed with PBS, re-suspended in 20mM HEPES (pH 7.4) containing protease inhibitor cocktail (dilution 1:100) (ThermoFisher Scientific) and sonicated on ice. Cells and tissue homogenates were centrifuged at 12,000g for 15 min. Cell or tissue supernatants (200 μ g

protein) were added to 50mM HEPES (pH 7.4) containing 100mM NaCl, 5mM EGTA, 1-SA-2-ETE-PE (7 μ M) or 1-SA-2-15-HpETE-PE (7 μ M) and incubated for 30 min at 37°C. For (S)-BEL-treatment, supernatants were pre-incubated with (S)-BEL (10 μ M), a chiral-specific non-reversible inhibitor of iPLA₂ β , for 10 min at 37°C. Reaction was stopped by chloroform:methanol (2:1, v/v), hydrolysis products were extracted and resolved by LC/MS. iPLA₂ β activity was expressed as pmols of 1-SA-2-OH-PE/min/mg of protein.

Western blot analysis.

Cells and tissues were resuspended in lysis buffer (25mM Tris-HCl, pH-7.5, 150mM NaCl, and 1% SDS) containing protease-phosphatase inhibitor cocktail (ThermoFisher Scientific), sonicated to break down DNA and total protein amount was estimated by BCA protein assay kit (ThermoFisher Scientific). Samples diluted in Laemmli buffer were loaded in 8–16% Tris-glycine gradient gels (Life Technologies), proteins transferred to nitrocellulose or polyvinylidene difluoride (PVDF) membranes (Bio-Rad) and blocked with 5% milk or BSA in PBST (0.1% Tween). Protein expression was detected using anti-iPLA₂ β (polyclonal, PA5-27945, Thermo Fisher Scientific), anti-tyrosine hydroxylase (ab112, abcam), anti- α -synuclein (SC-7011-R, Santa Cruz), anti-4-HNE (ab46545, abcam), anti-LPCAT3 (ProSci, 16-999; 1:500 dilution), anti-GAPDH (FD0063, Fude Biotech), and anti- β -actin (mouse monoclonal, A3854, clone AC-15, Sigma-Aldrich) antibodies (1% BSA in PBST) overnight at RT, washed 3 times, and incubated with horseradish peroxidase (HRP)-conjugated secondary antibody-goat anti-rabbit IgG (A0545, Sigma-Aldrich, FDR07, Fude Biotech) and goat anti-mouse IgG (FDM07, Fude Biotech) (1 hr) in blocking solution before developing with SuperSignal West Pico Chemiluminescent Substrate (Thermo Fisher Scientific). Bands were visualized using X-ray film or imaged using Amersham Imager 600 (GE Health Care, Life Sciences) and quantified using ImageJ software (NIH) (<https://imagej.nih.gov/ij/>). The integrated density value was obtained by integrating the entire pixel values in the area of one band after correction for background and then normalized to loading control (actin/GAPDH).

LC-MS/MS analysis of ETE and 15-HpETE.

ETE and 15-HpETE were analyzed by LC/MS using an Ultimate 3000 HPLC system coupled on-line to a Q-Exactive Hybrid Quadrupole-Orbitrap mass spectrometer (ThermoFisher Scientific) using a C18 column (Acclaim PepMap RSLC, 100Å, 5 μ m, 150 mm \times 0.3 mm, 35°C, ThermoFisher Scientific). Gradient solvents A (20% methanol) and B (90% methanol) contained 5 mM ammonium acetate. Flow rate was maintained at 12 μ l/min. The gradient was as follows: 30% solvent B to 95% solvent B, from 0–70 min, hold at 95%B from 70–80 min, 30%B from 80–83 min, 30%B from 83–90 min. Negative ion mode MS conditions were as follows: resolution, 140,000 for the full MS and data-dependent scan; scan range, m/z 150–600; isolation window 1.0 Da for MS and MS² scans; capillary spray voltage and temperature 2.6 kV and 250°C, respectively; S-lens - 60. Analytical data were acquired and analyzed using Xcalibur 4.2 Quan Browser (ThermoFisher Scientific).

LC-MS/MS analysis of 15-HpETE-PE.

Lipids were extracted and phosphorus was determined by a micro-method as described previously². Phospholipids were analyzed by LC/MS using an Ultimate 3000 HPLC system

coupled on-line to a Q-Exactive Hybrid Quadrupole-Orbitrap mass spectrometer (Thermo Fisher Scientific) or Orbitrap Fusion Lumos mass spectrometer (ThermoFisher Scientific) using a normal phase column (Luna 3 μm Silica (2) 100 \AA , 150 \times 1.0 mm, (Phenomenex)) as previously described². Q-Exactive negative ion mode MS conditions were as previously described². Fusion Lumos MS conditions: spray voltage, 4 kV; transfer tube temperature, 300 $^{\circ}\text{C}$; RF-Lens level, 50%. Data were acquired in data-dependant-MS² and targeted-MS³ mode. For MS: Ion detection, Orbitrap; mass resolution, 120,000; scan range, m/z 400–1800. For MS²: quadrupole isolation 1 Da; HCD, collision energy 24%; ion detection Orbitrap; mass resolution, 15,000. For MS³: isolation window, 2.0 Da; CID, collision energy, 35%; ion detection, ion trap. Analysis of raw LC/MS data was performed using Compound Discoverer™ 2.0 (ThermoFisher Scientific) with an in-house generated analysis workflow and database. Peaks with S/N ratio of more than 3 were identified and searched against oxidized phospholipids database. Lipids were further filtered by retention time and confirmed by MS³ analysis using the fragments utilized for their identification (www.Lipidmaps.org). Deuterated phospholipids (Avanti Polar Lipids) were used as internal standards. Values for m/z were matched within 5 ppm to identify the lipid species.

Analysis of oxygenated phospholipids by reverse phase LC/MS.

Total lipids were separated on an Thermo Ultimate 3000 LC system with a C30 reverse phase column (Accucore, 2.1mm \times 25 cm, 2.6 μm , ThermoFisher Scientific). Solvent A: Acetonitrile/water (50/50); Solvent B: 2-propanol/acetonitrile/water (85/10/5) contained 5mM ammonium formate and 0.1% formic acid as modifiers. Gradient was as follows: 0–20 min, 30%–70% B; 20–55 min, 70–100% B; 55–70 min, hold at 100% B; 70–85 min, 100–30% B; 85–95 min, 30% B for equilibration. The flow rate was 100 $\mu\text{L}/\text{min}$ and column temperature was 35 $^{\circ}\text{C}$. Analysis of phospholipids was performed on a Q-Exactive mass spectrometer (ThermoFisher Scientific). Negative ion mode MS conditions were as previously described⁹.

LC-MS analysis of catecholamine neurotransmitters and GSH.

Catecholamines and GSH were determined by LC-MS using a Triple Quad 4500 Mass Spectrometer (SCIEX) (Extended Data Table 3). Analytes were separated on a C18 column (Acquity HSS T3, 1.8 μm , 2.1 mm \times 100 mm, 40 $^{\circ}\text{C}$, Waters) at a flow rate of 0.4 mL/min on an Exion LC AD system. Gradient: solvent A (water) and solvent B (acetonitrile), each containing 0.1% formic acid (v/v): 0–1.2 min isocratic of 2% B, 1.2–2.5 min linear gradient of 2 to 60% B, 2.5–4.5 min linear gradient of 60% to 95% B, 4.5–5.0 min isocratic of 95% B, and 5.0–6.5 min re-equilibration of 2% B. Positive and negative ion modes switching with a scheduled MRM scan method was used. Capillary spray voltage: 5.5 and –4.5 kV; ion source temperature, 600 $^{\circ}\text{C}$. Nebulizer gas and heater gas was set to 55 psi, and curtain gas was set to 30 abr. Data acquisition and processing were carried out using Analyst 1.6.2 software (SCIEX).

Computational modeling of the full iPLA₂ β dimer structure.

iPLA₂ β structure (752 residues) complexed with ankyrin fragments was constructed using the available structure (PDB code: 6aun¹⁵) and a combination of homology modeling and *ab initio* simulations. The structures of the short missing fragments in the X-ray structure of

iPLA₂β dimer (UniProt ID: A0A384E119), i.e. Y95-R115, L129-N145, R405-K408 and V652-A670, were reconstructed using SWISS-MODEL⁴⁴ server and longer M1-A80 fragment of ANK repeats with I-tasser⁴⁵ server. Detailed information on the quality of the model (released by SWISS MODEL and I-TASSER servers) has been provided in Extended Data Fig. 6. The full structure atomic coordinates of iPLA₂β are shared as supplementary material.

Construction and equilibration of neuronal lipid bilayer.

Neuronal membrane containing 15-HpETE-PE (4%), ETE-PE (SAPE, 22%) and various phospholipids (SAPI-4%, SOPC-15%, PSPC-25%, SOPE-5%, OLPS-10%, PAPC-5%, SDPE-10%), the composition of which has been deduced from lipidomics data, has been prepared using CHARMM-GUI⁴⁶ and in-house scripts. The membrane size was 50×50×50Å. The same composition and spatial distribution have been replicated to construct larger membranes (100×100Å² and 250×250Å² surface area and 50Å depth) to avoid end effects. Equilibration simulations were performed for 50×50×50Å membrane using NAMD⁴⁷ software with CHARMM force field and explicit water model (TIP3P). The simulated system contained over 51,000 atoms, including the lipid and water molecules, and KCl ions. Six preparatory simulations were conducted before the main run following CHARMM-GUI protocols. Two main 100 ns MD simulations were performed where the additional polar oxygen atoms-containing acyl chains of ETE-PE reoriented and partially protruded from the membrane surface into the aqueous solution. Force field parameters for 15-HpETE-PE were created using SwissParam⁴⁸. The structural model of 15-HpETE-PE was built and minimized using Maestro.

Molecular Dynamics (MD) Simulations of iPLA₂β dynamics, bound to the lipid bilayer.

Equilibrated membrane with protruding acyl chain of 15-HpETE-PE was replicated to perform protein-membrane simulations. The dimeric protein orientation (CAT domain (M416-P752) and full structure of iPLA₂β (M1-P752)) in the membrane was predicted by PPM server⁴⁹. The systems contained over 320,000 atoms (100×100×115 Å box, CAT domains) and 750,000 atoms (200×200×125 Å, iPLA₂β dimer). The following protocol was adopted using NAMD package: 0.2 ns of water equilibration, 10,000 steps of minimization, 0.35 ns of heating from 0 to 300K, and 0.15 ns equilibration before initiating the production MD run. Eight trajectories (four for WT and R693W, each), with CAT domain dimer in close proximity to the membrane were generated, each 55 ns long with 2 fs timesteps. Four 20 ns trajectories with the full structure of iPLA₂β dimer were also computed. A cutoff of 12Å was adopted for non-bonded interactions. Langevin dynamics and Langevin piston algorithm were used to maintain the temperature at 300K and the pressure at 1 atm. Analysis was performed using VMD and *Pro Dy* API together with in-house codes⁵⁰.

in silico saturation mutagenesis analysis.

The tool Rhapsody²² developed for predicting the functional consequences of single amino acid variants (SAVs) was used for automated scanning of all iPLA₂β residue substitutions. The method uses a Random Forest-based classifier trained using an integrated dataset of 20,854 missense mutations functionally characterized to date. For each protein, eight

structural, sequence-based, and dynamics-based features are calculated using multiple approaches, requiring iPLA₂β structure (PDB id: 6aun) as input. The reported Rhapsody scores represent the probability of causing a deleterious effect on function²².

Behavioral studies.

Pole test: Pole test was used to evaluate the mouse movement disorder. The instrument consists of an iron stand (height, 60 cm; diameter, 0.8 cm) with a small ball wrapped with gauze at the top. Mice were placed on the top of a small ball and the time required for the mouse to climb down the pole was recorded. The test was measured 3 times/mouse and the maximum time was recorded.

Rotarod test: Rotarod performance was used to assess mouse motor balance and coordination. Mice were trained for 3 days prior to treatment to adapt to the rotarod apparatus (Zhenghua Co.). After training, on the 7th day, mice were placed in the separate runway on the rod and at a constant speed of 25 rpm every day at the same time. Each mouse was tested three times. The latency to fall was recorded.

Catwalk test: CatWalk Gait Analysis is a system for rodent gait analysis. The apparatus consists of a long glass walking plate, a fluorescent light beamed into the glass plate and a high-speed video camera under the glass plate. In a dark environment, the light was reflected downward and a camera mounted under the glass recorded the footprint of mouse on the walkway. Mice were trained to cross the glass walkway three days prior to the test. The mouse performed unforced and uninterrupted moving at least three times. The data of mouse gait was qualitatively and quantitatively analyzed by the automated gait analysis system CatWalk (Noldus Information Technology).

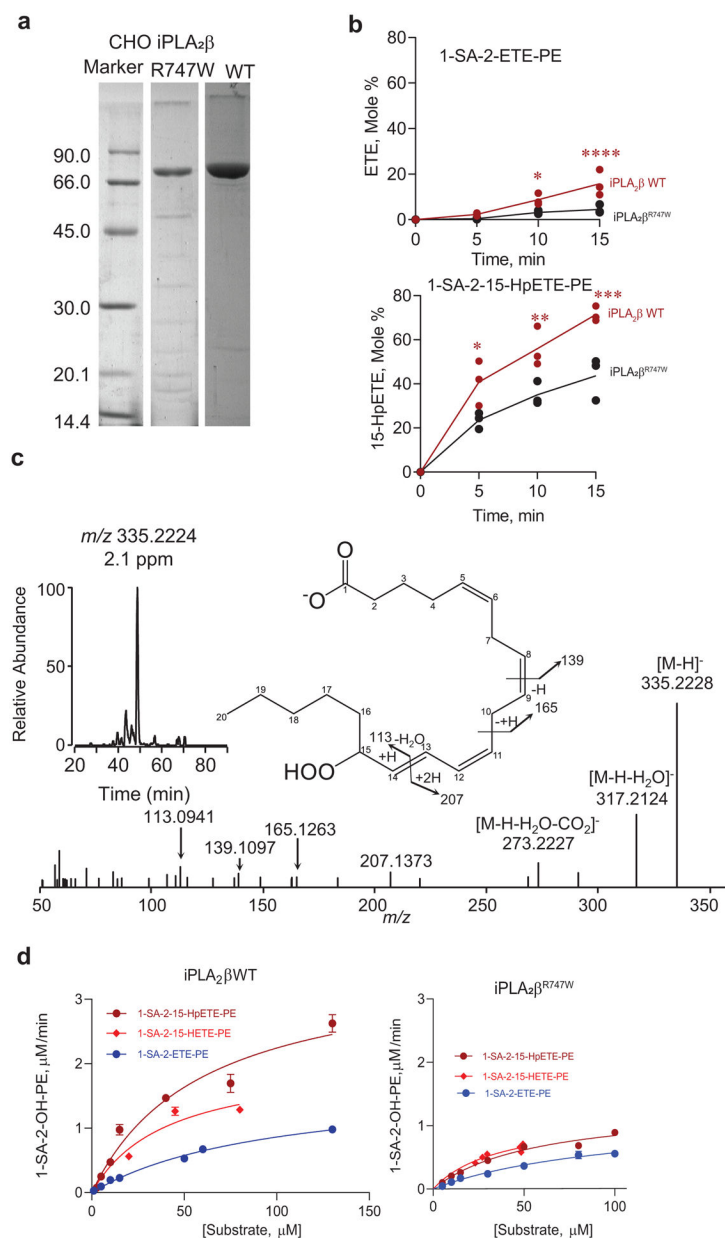
Statistical analysis.

The results are presented as mean±standard deviation (s.d.) with a minimum of three replicates unless otherwise specified. Statistical analyses were performed by either Student's *t*-test or one-way/two-way ANOVA for normally distributed data using Prism 8.1 (GraphPad Software, Inc). The significance of differences was set at $p<0.05$. When the overall ANOVA revealed a significant effect, the data were further analyzed with the Dunnett/Sidak post hoc test to determine specific group differences.

Data availability:

Data generated during the study and included in this article are available from the corresponding authors upon request.

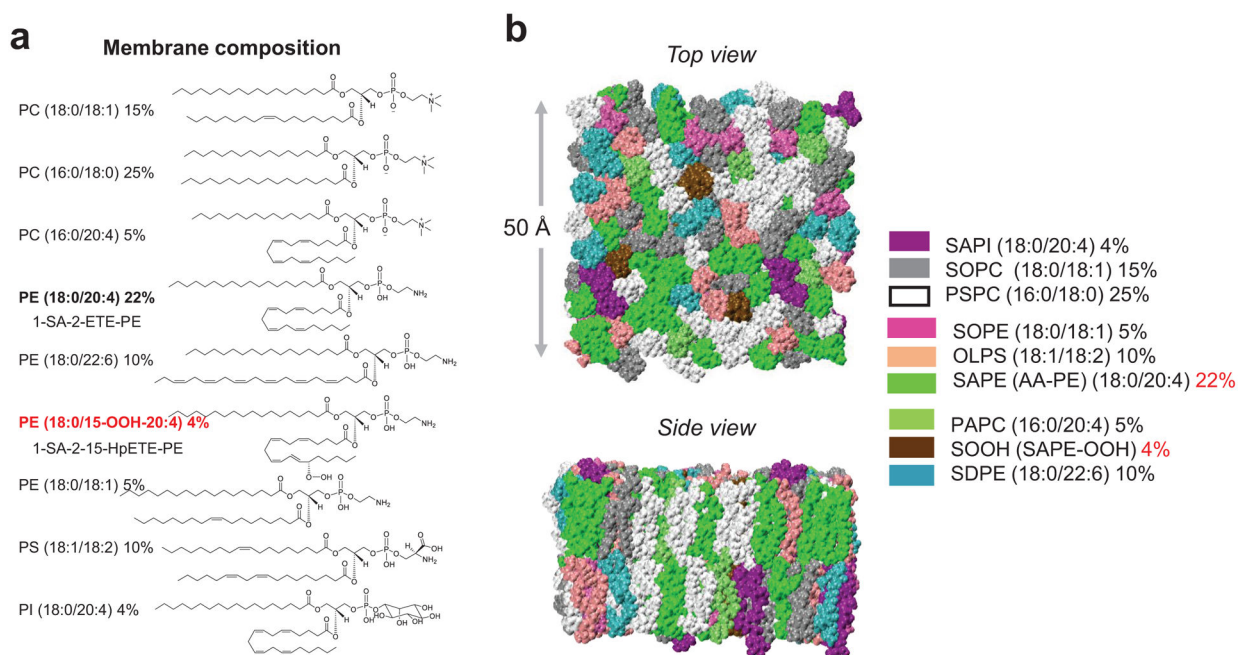
Extended Data



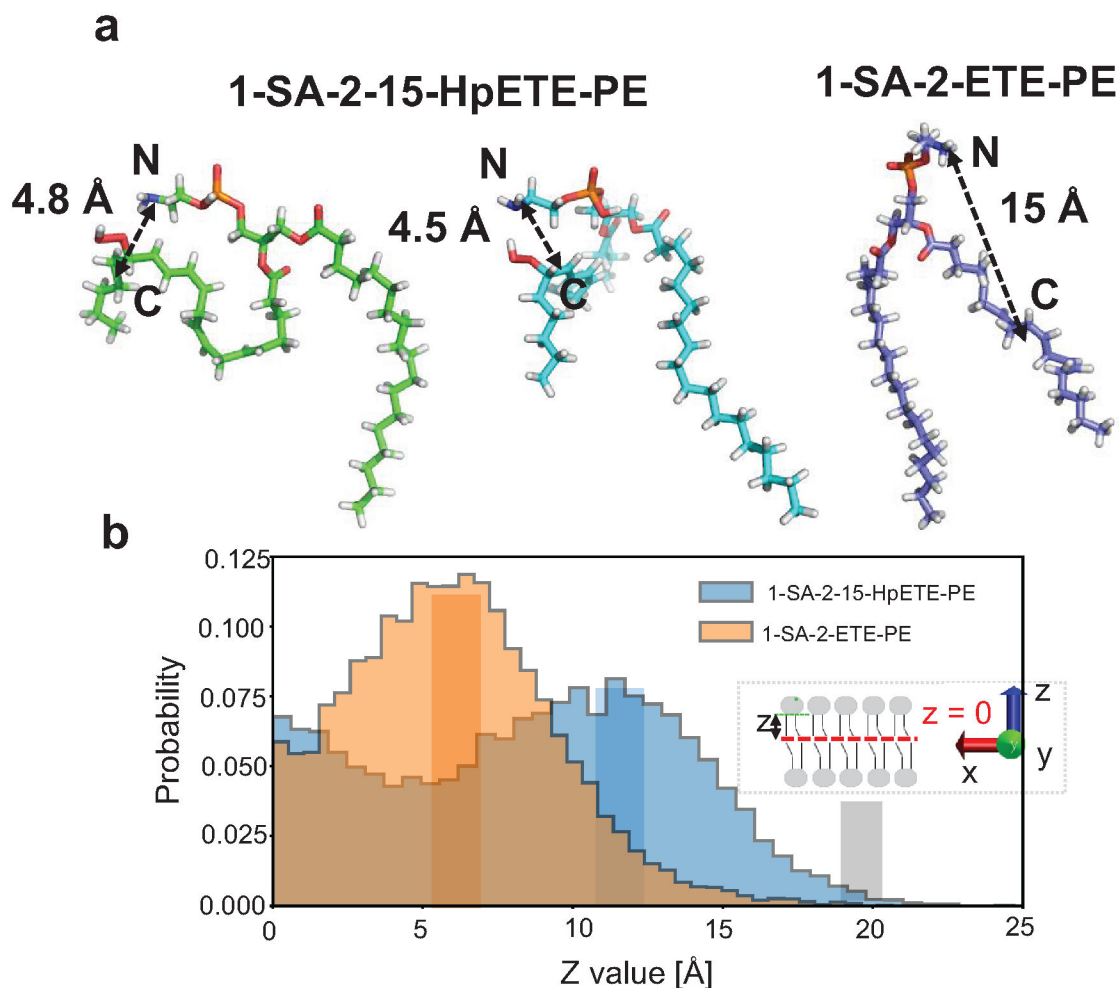
Extended Data Fig. 1. Purification of iPLA₂β and analysis of 15-HpETE and its hydrolysis products.

a, Western blot of purified recombinant WT and R693W mutant short variant CHO. The Short variant lacks a 54 amino acid (396–450) insert between ankyrin repeats and catalytic domain. The numbering is adjusted accordingly, such that R747W in Human Long iPLA₂β is R693W in the CHO construct. Representative figure from 3 experiments **b**, Time-courses of ETE (upper panel) and 15-HpETE (lower panel) formation in reactions catalyzed by mutant *R747W* (red circles) or WT iPLA₂β (black circles). 1-SA-2-ETE-PE and 1-SA-2-15-HpETE-PE were used as substrates. Data are means±s.d., N=3 independent experiments, **p*=0.0381, ****p*<0.0001 for 1-SA-2-ETE-PE data and **p* = 0.0189, ***p* = 0.0044, ****P* =

0.0003 for 1-SA-2-15-HpETE-PE data, WT iPLA₂β vs iPLA₂β^{R747W} at respective time points, two-way ANOVA (Sidak's post-hoc test). We employed highly purified (>99%) substrates (1-SA-2-ETE-PE and 1-SA-2-15-HpETE-PE) thus free ETE and free 15-HpETE were undetectable in the samples with no enzyme added. **c**, Detection and identification of 15-HpETE, a hydrolysis product of 1-SA-2-15-HpETE-PE. Base peak chromatogram of molecular ions with m/z 335.2224 corresponding to 1-SA-2-15-HpETE (*left* insert). MS² fragmentation pattern of molecular ions with m/z 335.2224 corresponding to 15-HpETE (*right* panel). Respective structure and fragments formed during MS² analysis (right insert). **d**, Effect of substrate concentration on the velocity of iPLA₂β WT (left panel) and iPLA₂β^{R474W} (right panel) catalyzed reaction. 1-SA-2-ETE-PE (blue circles), 1-SA-2-15-HETE-PE (light red circles) and 1-SA-2-15-HpETE-PE (dark red circles) were used as substrates. Data are presented as 1-SA-2-OH-PE mM/min, Data are means ± s.d, N=4 independent experiments for 1-SA-2-15HpETE-PE, 1-SA-2-15HETE-PE data and 3 for 1-SA-2-ETE-PE data.



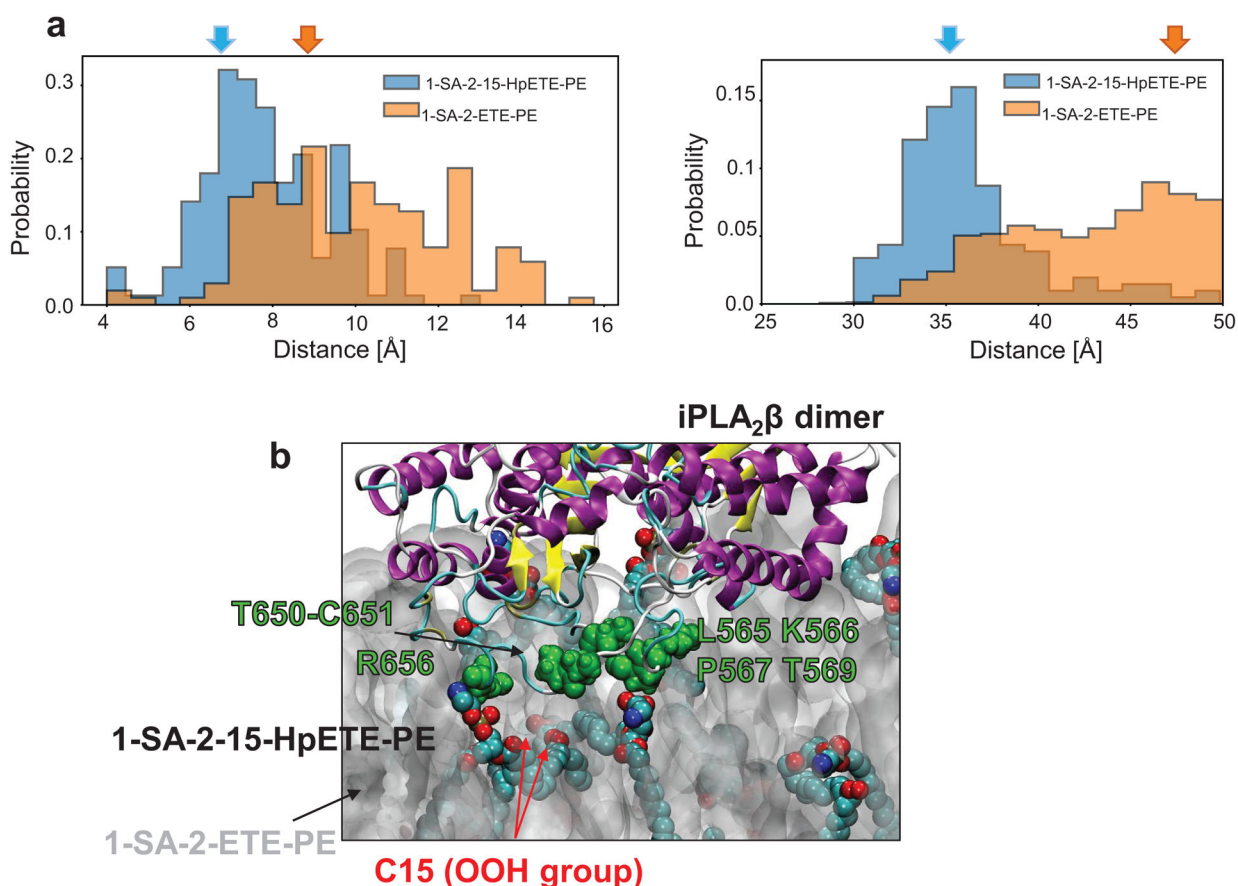
Extended Data Fig. 2. Membrane composition and atomic structure used in MD simulations. **a**, Structural formulas of phospholipids used in simulations. **b**, Spatial distribution in the lipid bilayer. The lipid composition has been deduced from our lipidomics data (see Methods) Here, SAPE is ETE-PE, and SOOH is 15-HpETE-PE. ETE-PE and 15-HpETE-PE were included at the levels of 22% and 4%, respectively. See legend at the *bottom* for the complete composition. The same composition and spatial distribution have been replicated to construct a larger membrane (100 × 100 Å² and 250 × 250 Å² surface area and 50 Å depth/thickness) in a simulation box with a height of 125 Å enclosing the dimeric enzyme bound to the membrane and explicit water molecules.



Extended Data Fig. 3. Comparison of conformational Flexibility of Acyl Chains.

a, Hydroperoxy-group in 15-HpETE-PE comes into close proximity of the membrane surface. Conformations reached in 100 ns MD simulations are shown for two 15-HpETE-PE molecules (*left and middle*) and one for ETE-PE (*right*). The distances between terminal amino group N-atom and the peroxidized C15-atom of the *sn*-2-acyl chain in 15-HpETE-PE and in ETE-PE (using the non-peroxidized equivalent C15-atom) are shown. A total of eight simulations were carried out, four with WT and four with mutant R747W iPLA₂β. This distance was < 5 Å in at least two 15-HpETE-PE out of the total of 20 per MD snapshot. No such a short distance was observed for ETE-PE. Results for the two sets of four runs were very similar, showing that the behavior of the fatty acid chains is intrinsic to the oxidized fatty acids, irrespective of the iPLA₂β. Similar behavior was also observed in the simulations of the membrane alone (in the absence of enzyme). The results in panel (a) are in qualitative agreement with the Nuclear Overhauser Effects (NOE) data obtained by Greenberg et al., 2007. The authors observed signals for irradiated -N(CH₃)₃ protons of the choline group and the terminal aldehydic group of the truncated *sn*-2-oxidized fatty acid chain in oxidized lipids, consistent with ‘whisker’ model. However, no signals were observed for non-oxidized lipids, as these were embedded within the hydrophobic bilayer. Observation of a signal in NOE experiments, corresponds to a distance of < 5 Å. **b**,

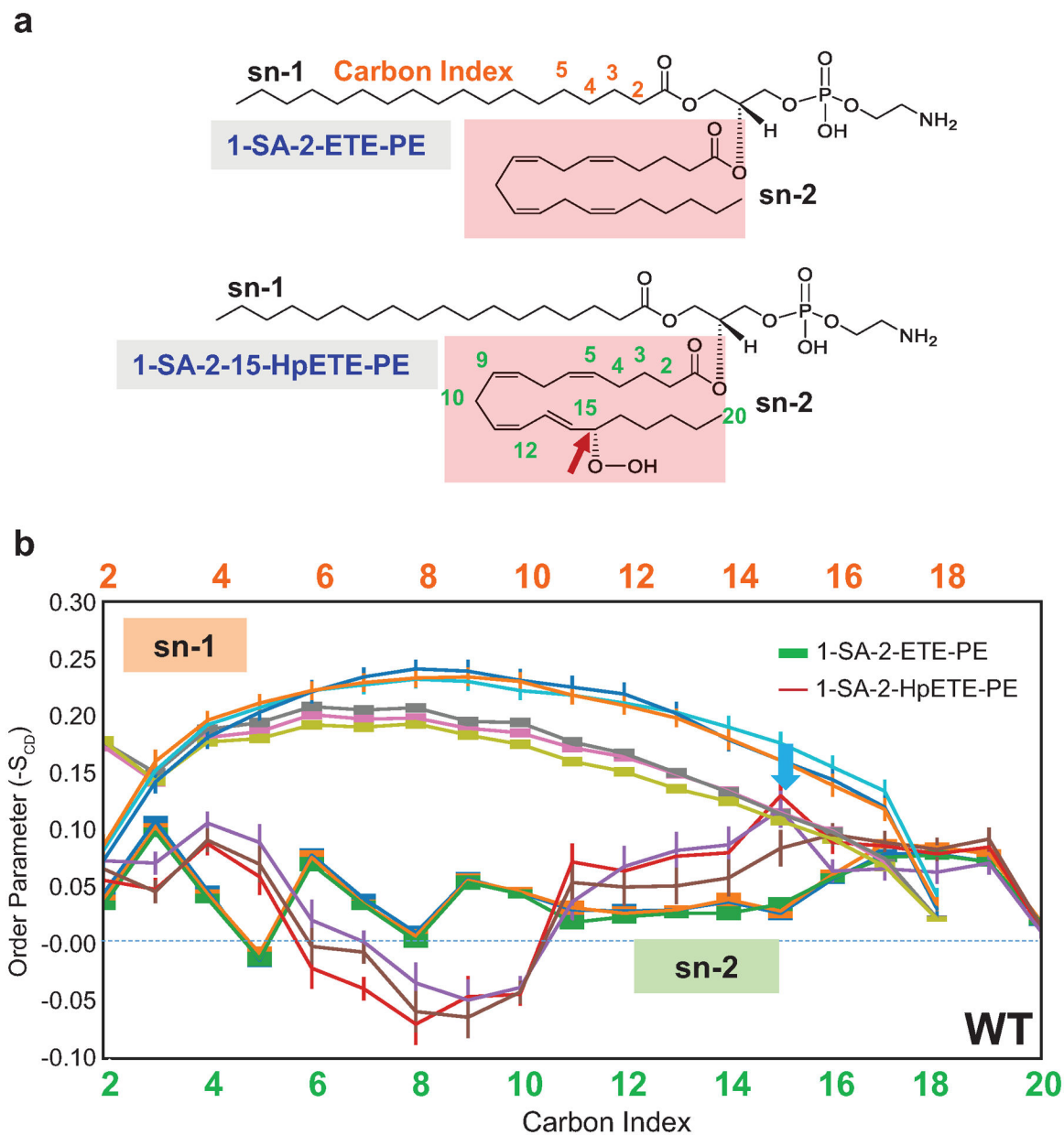
Probability distribution of the position of the peroxidized/non-peroxidized carbon (C15, *sn*-2) for 15-HpETE-PE and ETE-PE along the z-axis of the lipid bilayer. The interface between the two lipid monolayers (*red dotted line in the inset*) serves as a reference point ($z = 0$, shown in the *inset*) for the distances of C15 carbon atom from the center of the bilayer. Six random lipids for both, 15-HpETE-PE and ETE-PE, were chosen for the analysis. Carbon index (C15) refers to that shown on the chemical structure in Supplementary Fig. 5a. Shaded boxes denote the approximate range of distances at which maxima occur in the histograms. The C15 ETE-PE (*orange box*) remains embedded at $\sim 5\text{--}6\text{ \AA}$, the C15 of 15-HpETE-PE moves closer to the membrane surface at $12\text{--}13\text{ \AA}$ (*blue box*). The positions of the head groups at the membrane surface are indicated by *grey box*. The probability distributions show that the C15 atom (“peroxidized”) of 1-SA-2-15-HpETE-PE adopts two distinct positions, one close to the membrane surface (blue box) the other buried near the central part of the lipid bilayer ($z=0$).



Extended Data Fig. 4. Ability of the peroxidized group in 1-SA-2-HpETE-PE to come into close proximity of the protein surface.

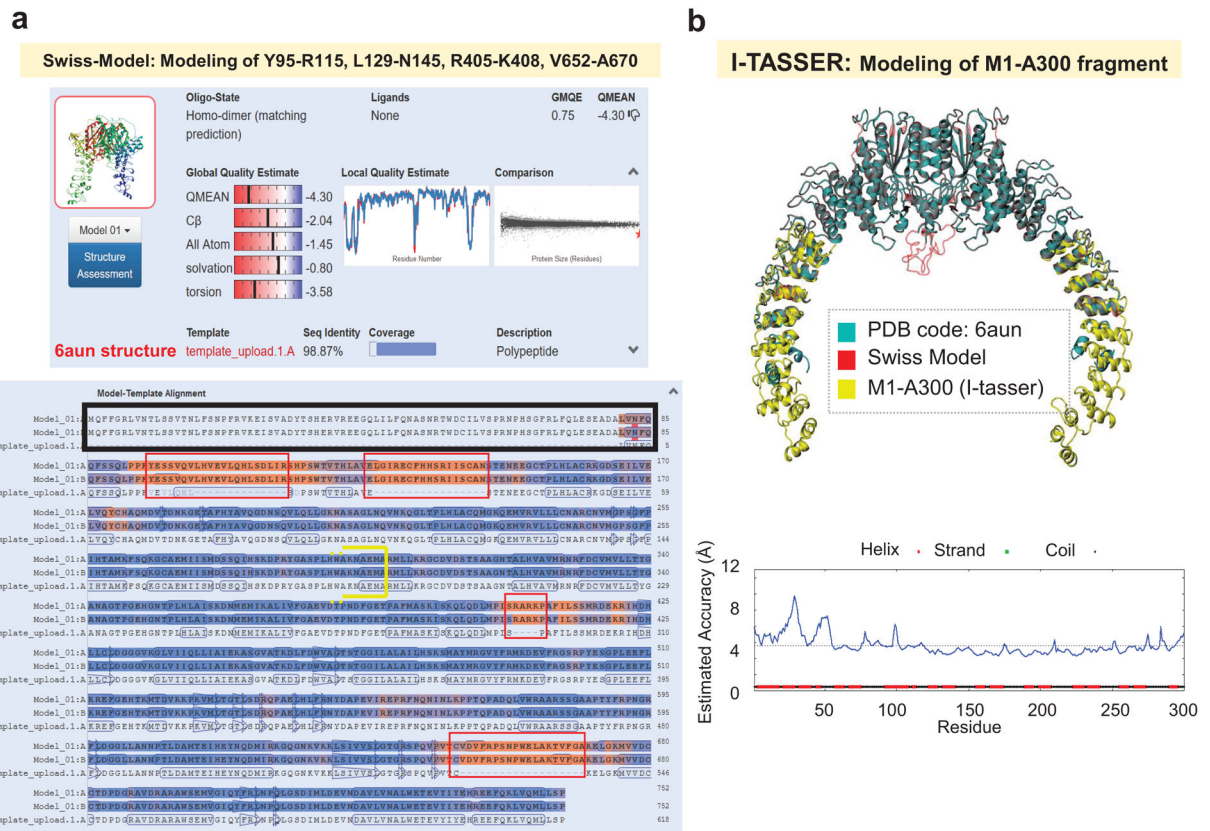
a, Probability distribution of the distance between the peroxidized carbon (C15, *sn*-2) of 1-SA-2-15-HpETE-PE or non-peroxidized carbon (C15, *sn*-2) of ETE-PE and: (i) protein surface (*left panel*) and (ii) catalytic site (*right panel*). For protein surface the closest atom of the lipid was taken into account whereas the reference point for catalytic site was computed based on the closest atom of the lipid to the center of mass of the highly conserved catalytic

residue S465 and D598. Carbon index (C15) refers to that shown on the chemical structure in Supplementary Fig. 5a. Arrows denote the maxima in the histograms for C15 (which contains the OOH group, shown in panel b) in 1-SA-2-15-HpETE-PE (*blue*) and C15 in ETE-PE (*orange*). The analysis contains results from the second half of three MD trajectories for a WT iPLA₂β dimer structure (50–100 ns period of time). **b**, A snapshot from MD simulations of iPLA₂β dimer CAT domains with residues making close contacts with 1-SA-2-15-HpETE-PE and 1-SA-2-ETE-PE highlighted in space filling representation (*green*). The 1-SA-2-15-HpETE-PE (*red-blue-cyan balls*) and ETE-PE (*grey surface*) in the membrane are shown.



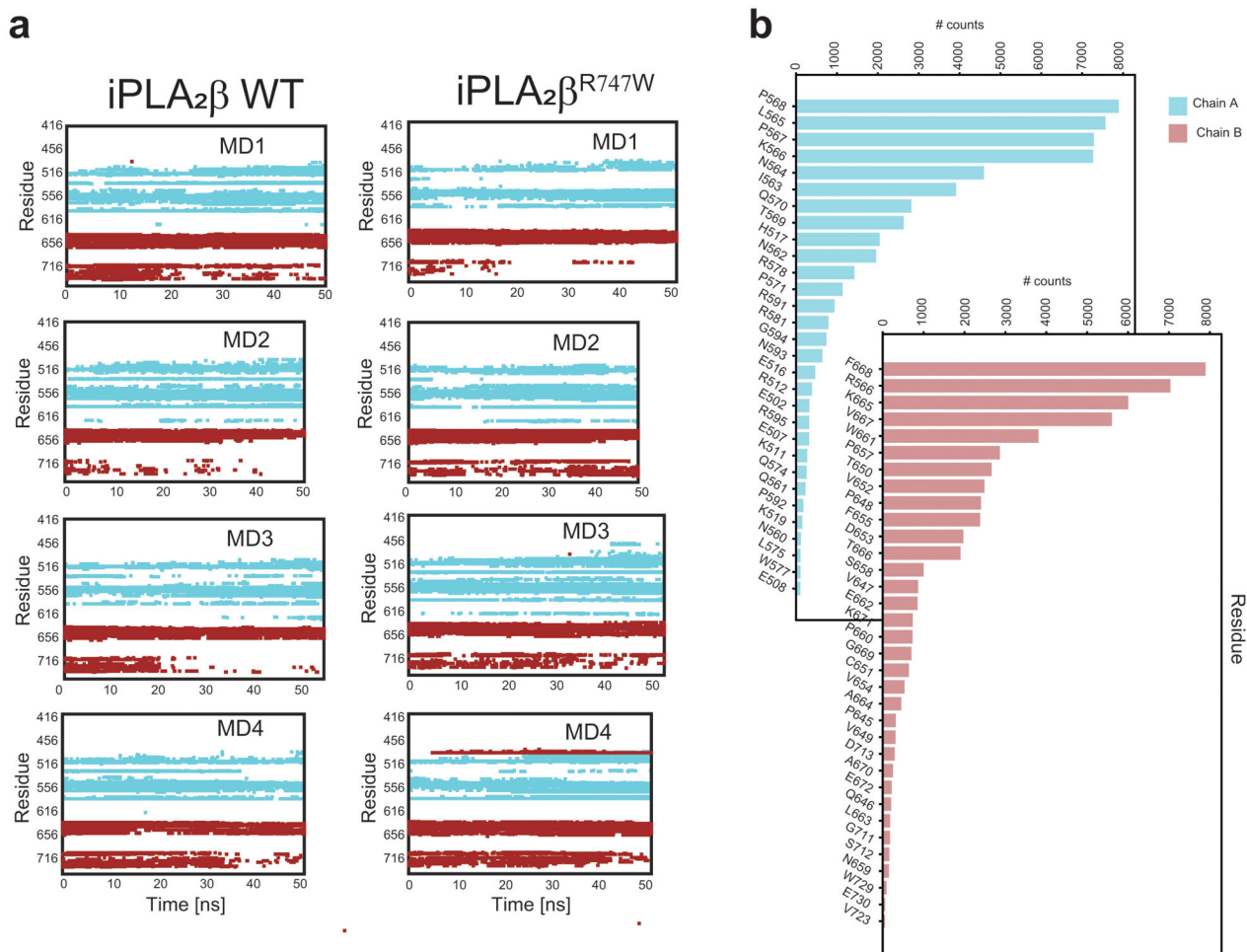
Extended Data Fig. 5. Comparison of the intrinsic dynamics of 1-SA-2-15-HpETE-PE and 1-SA-2-ETE-PE.

a, Chemical structures. Carbon atom indices are indicated in *green* for *sn-2* and *orange* for *sn-1*. *Pink boxes* highlight the *sn-2* chain which is different in the two lipids. *Blue arrow* points to the peroxidized carbon C15 in 1-SA-2-15-HpETE-PE. **b**, Order parameters computed from three sets of independent MD runs. Computationally predicted deuterium order parameters (SCD) for *sn-1* (*upper curves*) and *sn-2* (*lower curves*) chains, based on 3 MD runs performed for ETE-PE (*thick lines*) and three for 1-SA-2-15-HpETE-PE (*thin lines*). *Blue arrow* indicates position of C15. In general, the order parameter $S = 3/2 \langle \cos^2 \alpha \rangle - 1/2$ varies in the range $[-0.5, 1]$; the two limits corresponding to complete order (parallel alignment of the probed bond with respect to the magnetic field, with the angular difference being $\alpha = 0$) and antiparallel orientation ($\alpha = 90^\circ$). $S_{CD} = 0$ for fully disordered states ($\langle \cos^2 \alpha \rangle = 1/3$). The fully disordered state $S_{CD} = 0$ is shown by the dotted line. *Red arrow* shows the position of the oxidized carbon in 1-SA-2-15-HpETE-PE, where a slight increase in order is induced upon oxidation. Both chains display low order parameters, with the *sn-2* chain being more disordered in general than *sn-1*, except for the terminal C-atom of *sn-1* reflecting higher flexibility at the chain terminals. The results are shown for an ensemble of chains in each case, which exhibit highly reproducible patterns, also consistent with previous computational and experimental data. Note that the portion of 1-SA-2-15-HpETE-PE *sn-2* near the peroxidation site (C15) exhibit relatively higher ordering, whereas the remaining portions show a mixed behavior. While these differences are small, they are reproducible in independent runs, lending support to the robustness of simulation data. The computed order parameters values are in a good agreement with previously, reported computational and experimental values. Furthermore, while the published results on the effects of peroxidation on lipids dynamics are somewhat contradictory, our computational observations of the peroxidized *sn-2* acyl chains for 1-SA-2-15HpETE-PE are in general agreement with those computed for other peroxidized lipids using the same tools.



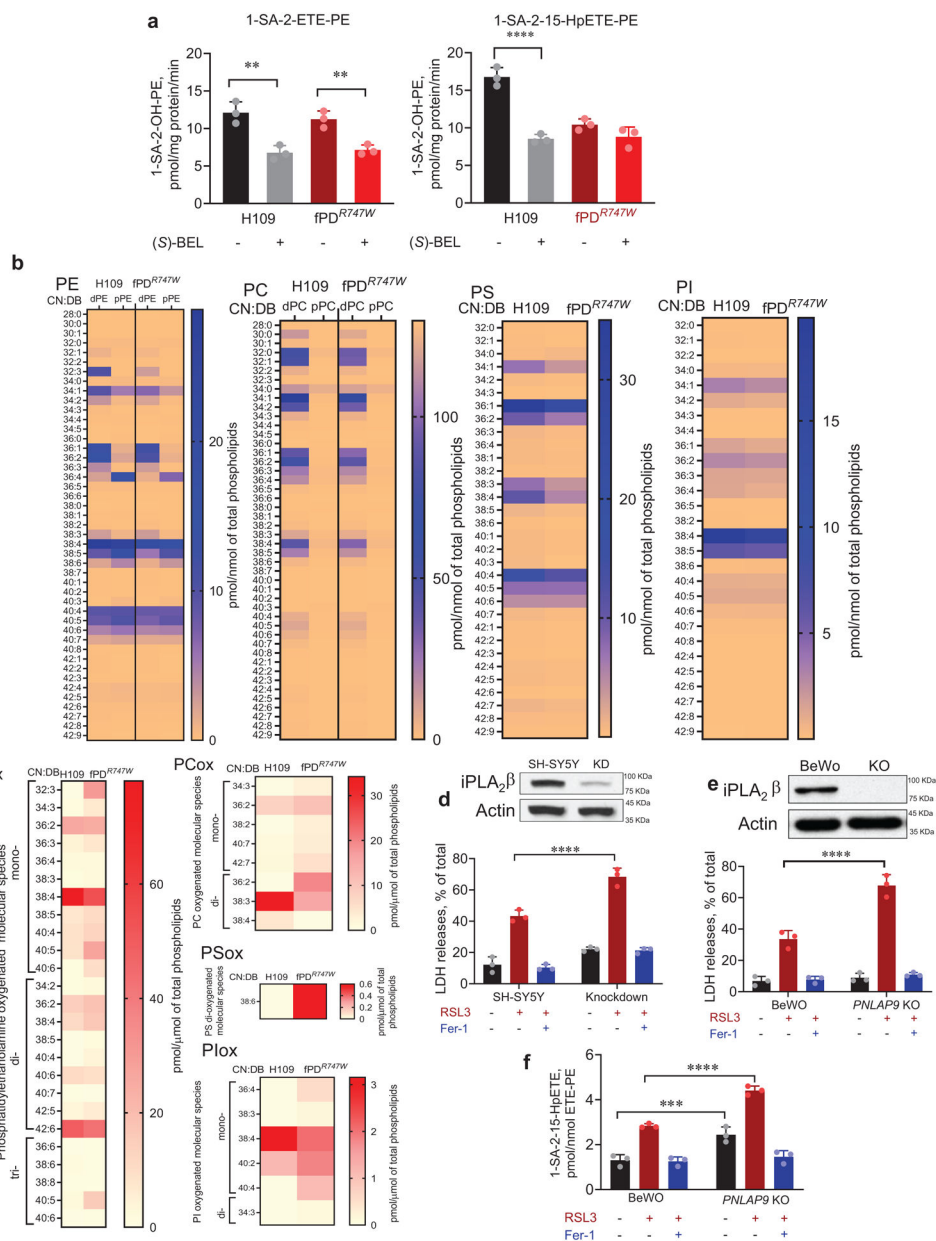
Extended Data Fig. 6. Homology modeling details of dimer iPLA₂β model.

a, *Swiss model* results for homology modeling which includes global and local quality estimate values, sequence identity and coverage compared to the protein template (PDB code: 6aun) and sequence alignment. *Red* boxes on the sequence alignment denote regions which was not solved in X-ray structure (6aun) and was modeled using Swiss model server i.e. Y95-R115, L129-N146, R405-K408, V652-A670. *Black box* highlight region M1-A80 which was not present in the ANK repeats fragment. **b**, I-tasser results for homolog modeling of M1-A300 fragment of iPLA₂β structure. *Cyan* ribbon diagram denote iPLA₂β dimer solved in X-ray (6aun), *red* elements of the structures were modeled using Swiss Model server (shown in the panel **a**, *red* boxes). M1-A300 fragment of ANK repeat is shown in *yellow* ribbon diagram and alignment on the crystal structure. Estimated accuracy obtained by I-tasser server for M1-A300 model is also shown.



Extended Data Fig. 7. Time evolution and histograms of interfacial contacts between iPLA₂ β residues and 15-HpETE-PE molecules observed in MD simulations.

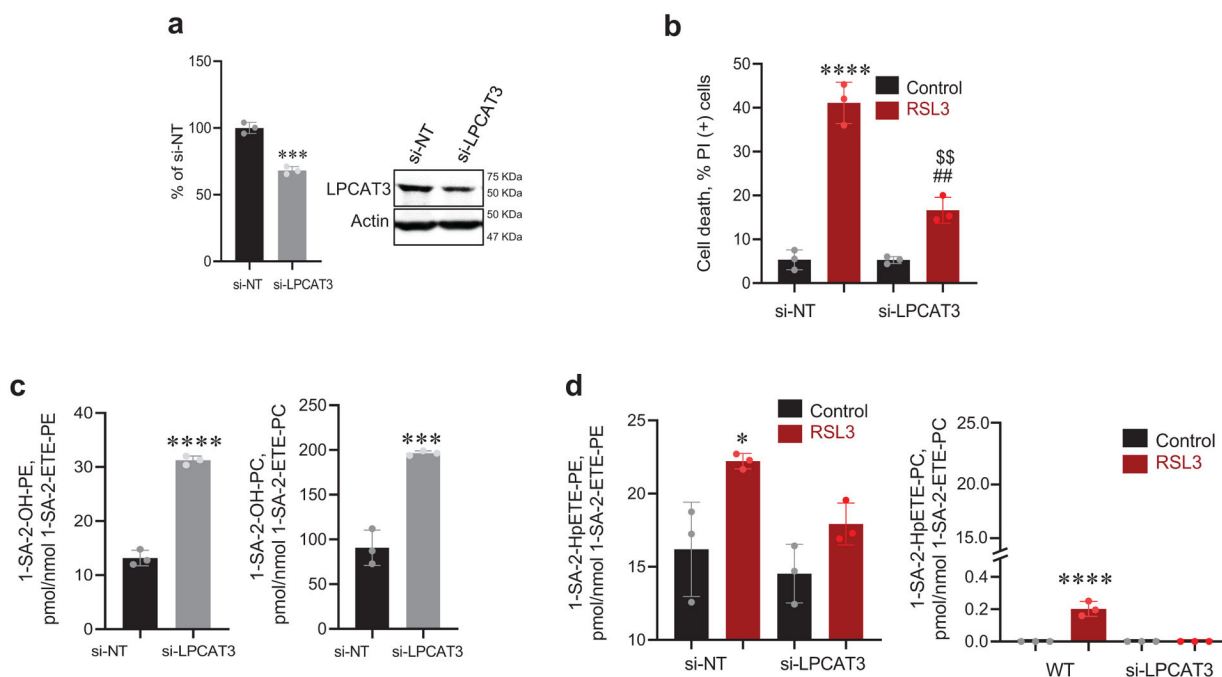
a) Results from 4×2 runs (labeled MD1–4) conducted for the WT and R747W mutants are displayed. Residues making contacts are listed along the ordinate, and the time evolution of contacts (atom-atom interactions closer than 3.5 Å with any 15-HpETE-PE atom) is shown in in each case. Colored regions indicate the contacts made by chain A (cyan) and B (dark red). Note that most of the contacts are persistent once formed. **b)** Histograms of contacts. Residues making the largest number of contacts (counts based on snapshots collected every 50 picoseconds, summed over all runs) are listed, along with the corresponding counts for chains A (*top*) and B (*bottom*).



Extended Data Fig. 8. iPLA₂β-deficient cells are more sensitive to RSL3-induced ferroptosis compared to WT cells.

a, Total PLA₂ activity in H109 and fPD^{R747W} cells in the absence and in the presence of (S)-BEL. Cell supernatants were incubated with 1-SA-2-ETE-PE (upper panel) or 1-SA-2-15-HpETE-PE (lower panel) for 30 min at 37°C. Activity is presented as 1-SA-2-OH-PE, pmol/min/mg protein. The background levels of 1-SA-2-OH-PE in H109 and fPD^{R747W} cell supernatants were low and estimated as 2.76 ± 0.19 and 2.74 ± 0.75 pmols per sample vs 70.5 ± 8.5 and 100.7 ± 10.5 pmols per sample accumulated in H109 and fPD^{R747W} cell supernatants during incubation in the absence of S-BEL. Data are means \pm s.d., * $p=0.0014$ for H109 cells, ** $p=0.0073$ for fPD^{R747W} cells, **** $p<0.0001$, $N=3$ biologically independent experiments, one-way ANOVA (Tukey post hoc test). **b**, Heat map showing the content of phosphatidylethanolamine (PE), phosphatidylcholine (PC), phosphatidylserine

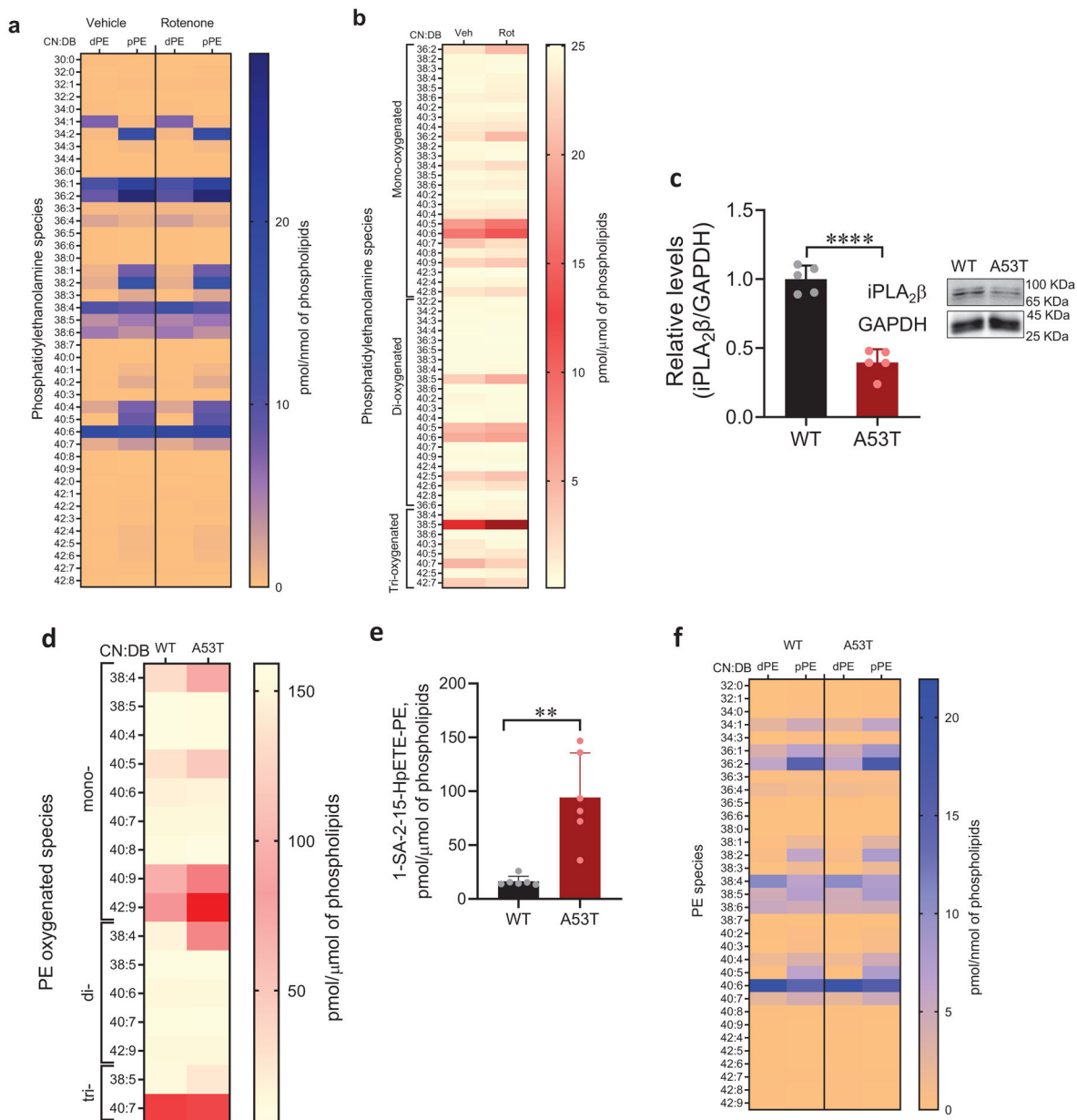
(PS) and phosphatidylinositol (PI) molecular species in H109 and fPD^{R747W} cells. dPE-diacyl species, pPE-plasmalogens, dPC-diacyl PC species, pPC-plasmalogen species of PC. Data presented as pmol/nmol of total phospholipids, N=3 biologically independent experiments. **c**, RSL3-induced accumulation of oxygenated PE (PEox, *left*), PC (PCox, *upper right*), PS (PSox, *middle right*) and PI (PIox, *lower right*) molecular species in H109 and fPD^{R747W} fibroblasts. Cells were exposed to RSL3 (25nM) for 14 hrs. Data presented as pmol/nmol of total phospholipids, N=3 biologically independent experiments. **d**, RSL3 - induced ferroptosis in WT and iPLA₂β KD SHSY5Y cells. Cell were treated with RSL3 (2 μM) for 18 hrs in the absence or in the presence of Fer-1 (0.4 μM). Inset: representative blot of iPLA₂β. Data are means±s.d., ****p<0.0001 vs WT, N=3 biologically independent experiments, two-way ANOVA (Sidak post-hoc test). **e**, RSL3-induced ferroptosis in WT and *PNPLA9* KO BeWo cells. Cells were incubated with RSL3 (100 nM) for 12 hrs in the absence or in the presence of Fer-1 (0.4 μM). Inset: Typical western blot of iPLA₂β obtained from BeWo WT and *PNPLA9* KO cells. Ferroptosis quantified by LDH release. Data are means±s.d., ****p<0.0001 vs WT, N=3 biologically independent experiments, two-way ANOVA (Sidak post-hoc test). **f**, Content of 1-SA-2-15-HpETE-PE in WT and *PNPLA9* KO BeWo cells. Data are means ± s.d., ***p=0.0002, ****p<0.0001 vs WT, N=3 biologically independent experiments, two-way ANOVA (Sidak post-hoc test).



Extended Data Fig. 9. LPCAT3 KD protects mouse embryonic cells from RSL3 induced death.

a, Representative immunoblots and quantification of LPCAT3 in cell treated with non-targeted siRNA (si-NT) or LPCAT3 siRNA (si-LPCAT3). LPCAT3 levels were quantified from three biological replicates and normalized to actin. Data represent mean ± s.d., *p=0.0004 vs si-NT, unpaired two-tailed *t*-test. **b**, si-NT or LPCAT3 KD cells were exposed to RSL3 (100 nM) and cell death was monitored after 20 hrs by PI staining using flow cytometry. Data are mean ± s.d., N=3 biologically independent experiments; ****p<0.0001

vs si-NT control, $^{###}p=0.0081$ vs si-LPCAT3 control, $^{$$$}p=0.0078$ vs si-NT/RSL3, one-way ANOVA. **c**, Quantitative LC/MS-based assessments of lyso-PE (1-SA-2-OH-PE, *left*) and lyso-PC (1-SA-2OH-PC, *right*) in MEF cells. Data are mean \pm s.d., N=3 biologically independent experiments, $^{***}p=0.0008$, $^{****}p<0.0001$ vs si-NT, unpaired two-tailed student's *t*-test. **d**, The contents of oxygenated PE (1-SA-2-HpETE-PE, *left*) and PC (1-SA-2-15-HpETE-PC, *right*) in MEF cells. Cells were exposed to RSL3 (100nM) for 20 hrs. Data are mean \pm s.d., N=3 biologically independent experiments, $^{*}p=0.0282$, $^{****}p<0.0001$ vs si-NT control, one-way ANOVA, (Tukey's post-hoc test).



Extended Data Fig. 10. Content of PE, oxygenated PE in midbrain of rotenone exposed rats and 8-months old WT and A53T mice.

a, Content of PE in substantia nigra of control rats (treated with vehicle, DMSO) and Parkinsonian rats (treated with rotenone for 14 days at a dose of 3mg/kg/day). Data are presented as pmol/nmol of total phospholipids, N=6 biologically independent animals. d-diacyl species; p-alkenyl (plasmalogen) species. **b**, Quantification of oxygenated PE species in substantia nigra of control rats (treated with vehicle, DMSO) and Parkinsonian rats (treated with rotenone for 14 days at the dose of 3mg/kg/day). Data presented as pmol/mmol of total phospholipids, N=6 biologically independent animals. **c**, iPLA₂β protein expression in midbrain of 8-months old WT and A53T mice. Inset: Typical western blot of iPLA₂β. Data are means ± SD, ****p <0.0001, N = 5 biologically independent animals, unpaired two-tailed Student's *t*-test. **d**, Content of oxygenated PE species in midbrains of WT and A53T mice. Data are presented as pmol/mmol of total phospholipids. **e**, Content of 15-HpETE-PE in midbrains of WT and A53T mice. Data are presented as pmol of 1-SA-2-15-HpETE-PE per mmol of total phospholipids, **p=0.0010 WT vs A53T mice, unpaired two-tailed Student's *t*-test. N= 6 biologically independent animals. **f**, Content of PE in midbrains of WT and A53T mice. Data are presented as pmol/nmol of total phospholipids, N=5 biologically independent animals. d-diacyl species; p-alkenyl (plasmalogen) species

Supplementary Material

Refer to Web version on PubMed Central for supplementary material.

ACKNOWLEDGEMENTS:

This work was supported by NIH (HL114453, AI156924, AI156923, CA165065, CA243142, AI145406, NS076511, NS061817, P41GM103712, R21NS094854, PA30DA035778 and P01DK096990), Natural Science Foundation of China (81873209, 81622050, 81903821), National Science Centre, Poland (Grant 2019/35/D/ST4/02203), 111 Project of Chinese MoE (B13038), the Local Innovative and Research Teams Project of Guangdong Pearl River Talents Program (2017BT01Y036), GDUPS (2019), and the March of Dimes Prematurity Research Center at the University of Pennsylvania. We are grateful to Jennifer Guererro-Santoro for technical assistance with the PNPLA9 KO BeWo cells.

REFERENCES

- Galluzzi L et al. Molecular mechanisms of cell death: recommendations of the Nomenclature Committee on Cell Death 2018. *Cell Death Differ* 25, 486–541 (2018). [PubMed: 29362479]
- Kagan VE et al. Oxidized arachidonic and adrenic PEs navigate cells to ferroptosis. *Nat Chem Biol* 13, 81–90 (2017). [PubMed: 27842066]
- Dixon SJ et al. Ferroptosis: an iron-dependent form of nonapoptotic cell death. *Cell* 149, 1060–1072 (2012). [PubMed: 22632970]
- Stoyanovsky DA et al. Iron catalysis of lipid peroxidation in ferroptosis: Regulated enzymatic or random free radical reaction? *Free Radic Biol Med* 133, 153–161 (2019). [PubMed: 30217775]
- Ursini F, Maiorino M, Valente M, Ferri L & Gregolin C Purification from pig liver of a protein which protects liposomes and biomembranes from peroxidative degradation and exhibits glutathione peroxidase activity on phosphatidylcholine hydroperoxides. *Biochim Biophys Acta* 710, 197–211 (1982). [PubMed: 7066358]
- Kapralov AA et al. Redox lipid reprogramming commands susceptibility of macrophages and microglia to ferroptotic death. *Nat Chem Biol* 16, 278–290 (2020). [PubMed: 32080625]
- Stockwell BR et al. Ferroptosis: A Regulated Cell Death Nexus Linking Metabolism, Redox Biology, and Disease. *Cell* 171, 273–285 (2017). [PubMed: 28985560]

8. Anthonymuthu TS et al. Empowerment of 15-Lipoxygenase Catalytic Competence in Selective Oxidation of Membrane ETE-PE to Ferroptotic Death Signals, HpETE-PE. *J Am Chem Soc* 140, 17835–17839 (2018). [PubMed: 30525572]
9. Wenzel SE et al. PEBP1 Wardens Ferroptosis by Enabling Lipoxygenase Generation of Lipid Death Signals. *Cell* 171, 628–641 e626 (2017). [PubMed: 29053969]
10. Liu GY et al. The phospholipase iPLA2gamma is a major mediator releasing oxidized aliphatic chains from cardiolipin, integrating mitochondrial bioenergetics and signaling. *J Biol Chem* 292, 10672–10684 (2017). [PubMed: 28442572]
11. Guiney SJ, Adlard PA, Bush AI, Finkelstein DI & Ayton S Ferroptosis and cell death mechanisms in Parkinson's disease. *Neurochem Int* 104, 34–48 (2017). [PubMed: 28082232]
12. Mahoney-Sanchez L et al. Ferroptosis and its potential role in the physiopathology of Parkinson's Disease. *Prog Neurobiol*, 101890 (2020). [PubMed: 32726602]
13. Kautner KM, Hoft C, Rissling I, Oertel WH & Moller JC The PLA2G6 gene in early-onset Parkinson's disease. *Mov Disord* 26, 2415–2417 (2011). [PubMed: 21812034]
14. Zygogianni O et al. In Vivo Phenotyping of Familial Parkinson's Disease with Human Induced Pluripotent Stem Cells: A Proof-of-Concept Study. *Neurochem Res* 44, 1475–1493 (2019). [PubMed: 30989481]
15. Malley KR et al. The structure of iPLA2beta reveals dimeric active sites and suggests mechanisms of regulation and localization. *Nat Commun* 9, 765 (2018). [PubMed: 29472584]
16. Greenberg ME et al. The lipid whisker model of the structure of oxidized cell membranes. *J Biol Chem* 283, 2385–2396 (2008). [PubMed: 18045864]
17. Piggot TJ, Allison JR, Sessions RB & Essex JW On the Calculation of Acyl Chain Order Parameters from Lipid Simulations. *J Chem Theory Comput* 13, 5683–5696 (2017). [PubMed: 28876925]
18. Mohammadyani D et al. Molecular speciation and dynamics of oxidized triacylglycerols in lipid droplets: Mass spectrometry and coarse-grained simulations. *Free Radic Biol Med* 76, 53–60 (2014). [PubMed: 25110833]
19. Guo YP, Tang BS & Guo JF PLA2G6-Associated Neurodegeneration (PLAN): Review of Clinical Phenotypes and Genotypes. *Front Neurol* 9, 1100 (2018). [PubMed: 30619057]
20. Jenkins CM, Han X, Mancuso DJ & Gross RW Identification of calcium-independent phospholipase A2 (iPLA2) beta, and not iPLA2gamma, as the mediator of arginine vasopressin-induced arachidonic acid release in A-10 smooth muscle cells. Enantioselective mechanism-based discrimination of mammalian iPLA2s. *J Biol Chem* 277, 32807–32814 (2002). [PubMed: 12089145]
21. Paisan-Ruiz C et al. Characterization of PLA2G6 as a locus for dystonia-parkinsonism. *Ann Neurol* 65, 19–23 (2009). [PubMed: 18570303]
22. Ponzoni L, Penaherrera DA, Oltvai ZN & Bahar I Rhapsody: Predicting the pathogenicity of human missense variants. *Bioinformatics* 144, 279–292 (2020).
23. Panov A et al. Rotenone model of Parkinson disease: multiple brain mitochondria dysfunctions after short term systemic rotenone intoxication. *J Biol Chem* 280, 42026–42035 (2005). [PubMed: 16243845]
24. Iwata A, Maruyama M, Kanazawa I & Nukina N alpha-Synuclein affects the MAPK pathway and accelerates cell death. *J Biol Chem* 276, 45320–45329 (2001). [PubMed: 11560921]
25. Doll S et al. ACSL4 dictates ferroptosis sensitivity by shaping cellular lipid composition. *Nat Chem Biol* 13, 91–98 (2017). [PubMed: 27842070]
26. Doll S et al. FSP1 is a glutathione-independent ferroptosis suppressor. *Nature* 575, 693–698 (2019). [PubMed: 31634899]
27. Bersuker K et al. The CoQ oxidoreductase FSP1 acts parallel to GPX4 to inhibit ferroptosis. *Nature* 575, 688–692 (2019). [PubMed: 31634900]
28. Lands WE Metabolism of glycerolipids. 2. The enzymatic acylation of lysolecithin. *J Biol Chem* 235, 2233–2237 (1960). [PubMed: 14413818]
29. Hooks SB & Cummings BS Role of Ca²⁺-independent phospholipase A2 in cell growth and signaling. *Biochem Pharmacol* 76, 1059–1067 (2008). [PubMed: 18775417]

30. Astudillo AM, Balboa MA & Balsinde J Selectivity of phospholipid hydrolysis by phospholipase A2 enzymes in activated cells leading to polyunsaturated fatty acid mobilization. *Biochim Biophys Acta Mol Cell Biol Lipids* 1864, 772–783 (2019). [PubMed: 30010011]
31. Cedars A, Jenkins CM, Mancuso DJ & Gross RW Calcium-independent phospholipases in the heart: mediators of cellular signaling, bioenergetics, and ischemia-induced electrophysiologic dysfunction. *J Cardiovasc Pharmacol* 53, 277–289 (2009). [PubMed: 19390346]
32. Song H, Wohltmann M, Tan M, Ladenson JH & Turk J Group VIA phospholipase A2 mitigates palmitate-induced beta-cell mitochondrial injury and apoptosis. *J Biol Chem* 289, 14194–14210 (2014). [PubMed: 24648512]
33. Rodriguez Diez G, Uranga RM, Mateos MV, Giusto NM & Salvador GA Differential participation of phospholipase A2 isoforms during iron-induced retinal toxicity. Implications for age-related macular degeneration. *Neurochem Int* 61, 749–758 (2012). [PubMed: 22732705]
34. van Leeuwen EM et al. A new perspective on lipid research in age-related macular degeneration. *Prog Retin Eye Res* 67, 56–86 (2018). [PubMed: 29729972]
35. Dexter D et al. Lipid peroxidation as cause of nigral cell death in Parkinson's disease. *Lancet* 2, 639–640 (1986).
36. Zhou Q et al. Impairment of PARK14-dependent Ca²⁺ signalling is a novel determinant of Parkinson's disease. *Nat Commun* 7, 10332 (2016). [PubMed: 26755131]
37. Matys V et al. TRANSFAC and its module TRANSCompel: transcriptional gene regulation in eukaryotes. *Nucleic Acids Res* 34, D108–110 (2006). [PubMed: 16381825]
38. Mori A et al. Parkinson's disease-associated iPLA2-VIA/PLA2G6 regulates neuronal functions and alpha-synuclein stability through membrane remodeling. *Proc Natl Acad Sci U S A* 116, 20689–20699 (2019). [PubMed: 31548400]
39. Jenkins CM et al. Identification, cloning, expression, and purification of three novel human calcium-independent phospholipase A2 family members possessing triacylglycerol lipase and acylglycerol transacylase activities. *J Biol Chem* 279, 48968–48975 (2004). [PubMed: 15364929]
40. Sanchez Campos S, Alza NP & Salvador GA Lipid metabolism alterations in the neuronal response to A53T alpha-synuclein and Fe-induced injury. *Arch Biochem Biophys* 655, 43–54 (2018). [PubMed: 30098984]
41. Zhou Z et al. Adipose-Specific Lipin-1 Overexpression Renders Hepatic Ferroptosis and Exacerbates Alcoholic Steatohepatitis in Mice. *Hepatol Commun* 3, 656–669 (2019). [PubMed: 31061954]
42. Greenamyre JT, Cannon JR, Drolet R & Mastroberardino PG Lessons from the rotenone model of Parkinson's disease. *Trends Pharmacol Sci* 31, 141–142; author reply 142–143 (2010). [PubMed: 20096940]
43. Kinghorn KJ et al. Loss of PLA2G6 leads to elevated mitochondrial lipid peroxidation and mitochondrial dysfunction. *Brain* 138, 1801–1816 (2015). [PubMed: 26001724]
44. Waterhouse A et al. SWISS-MODEL: homology modelling of protein structures and complexes. *Nucleic Acids Res* 46, W296–W303 (2018). [PubMed: 29788355]
45. Roy A, Kucukural A & Zhang Y I-TASSER: a unified platform for automated protein structure and function prediction. *Nature protocols* 5, 725–738 (2010). [PubMed: 20360767]
46. Jo S, Lim JB, Klauda JB & Im W CHARMM-GUI Membrane Builder for mixed bilayers and its application to yeast membranes. *Biophysical Journal* 97, 50–58 (2009). [PubMed: 19580743]
47. Phillips J et al. Scalable molecular dynamics with NAMD. *J. Comput. Chem* 26, 1781–1802 (2005). [PubMed: 16222654]
48. Zoete V, Cuendet MA, Grosdidier A & Michielin O SwissParam: a fast force field generation tool for small organic molecules. *J. Comp. Chem* 32, 2359–2368 (2011). [PubMed: 21541964]
49. Lomize MA, Pogozheva ID, Joo H, Mosberg HI & Lomize AL OPM database and PPM web server: resources for positioning of proteins in membranes. *Nucl. Aci. Res* 40, D370–D376 (2011).
50. Humphrey W, Dalke A & Schulten K VMD: visual molecular dynamics. *J Mol Graph* 14, 33–38, 27–38 (1996). [PubMed: 8744570]

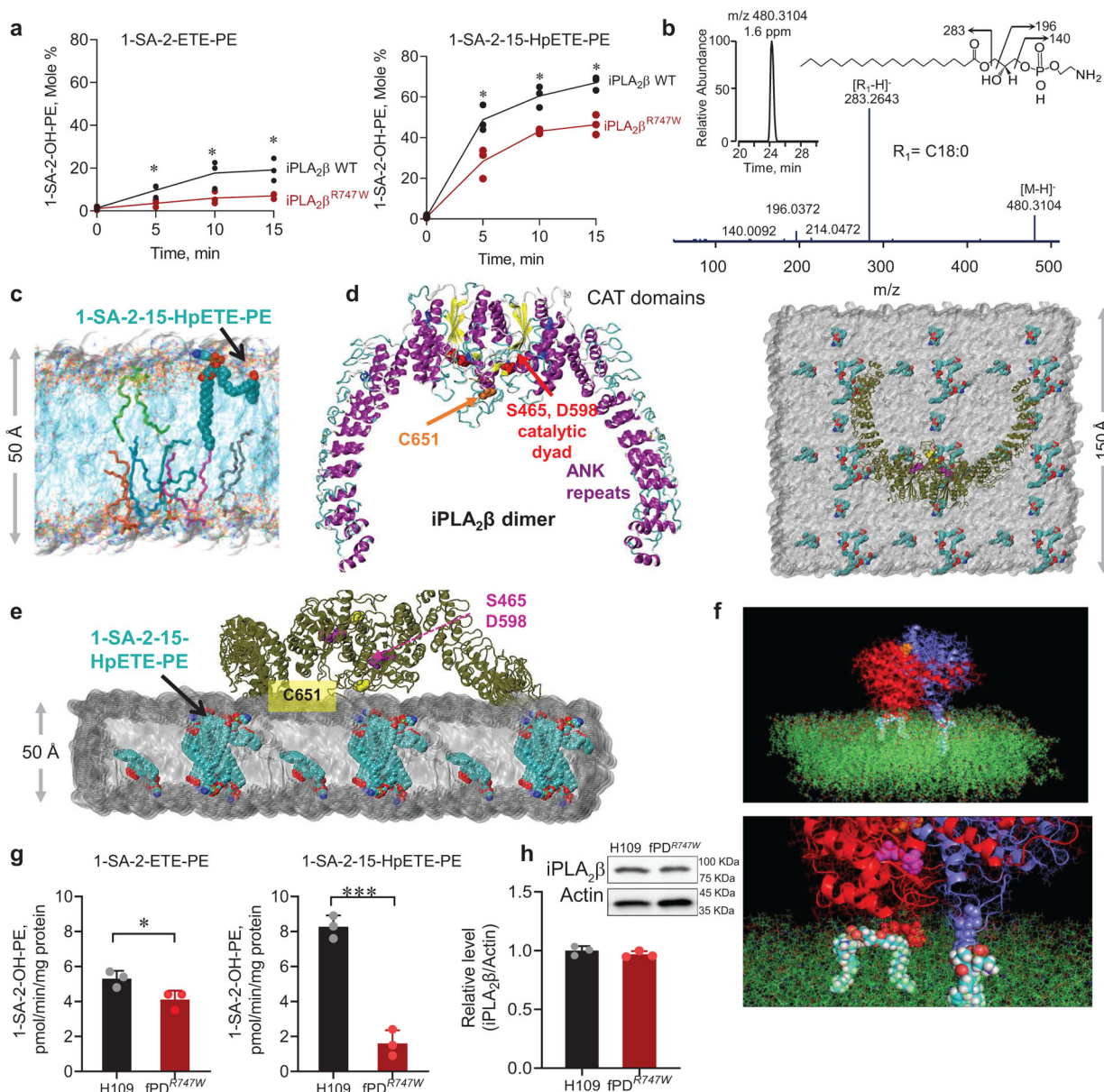


Fig. 1. Effect of point mutation on iPLA₂β function.

a, Time course of the formation of 1-SA-2-OH-PE in reactions catalyzed by iPLA₂β^{R747W} mutant (red circles) or WT iPLA₂β (black circles). 1-SA-2-ETE-PE (left) and 1-SA-2-15-HpETE-PE (right) were used as substrates. Data are means ± s.d., *p < 0.03, N = 3 independent experiments, two-tailed student's t-test. We employed highly purified (>99%) substrates (1-SA-2-ETE-PE and 1-SA-2-15-HpETE-PE) thus 1-SA-2-OH-PE was undetectable in the samples with no enzyme added. **b**, Detection and identification of 1-SA-2-OH-PE, a hydrolysis product of 1-SA-2-ETE and 1-SA-2-15-HpETE-PE. MS² fragmentation pattern of molecular ions with m/z 480.3104 corresponding to 1-SA-2-OH-PE. Inserts: Base peak chromatogram of molecular ions with m/z 480.3104 corresponding to 1-SA-2-OH-PE (left). Respective structure and fragments formed during MS² analysis (right). Indicated m/z values: 480 - precursor ion [M-H]⁻, 283 - sn1-RCOO⁻ ion, 214 - loss of sn1 acyl chain as

ketene ($\text{RCH}=\text{C}=\text{O}$) from $[\text{M}-\text{H}]^-$, 196 - neutral loss of sn1 RCOOH group from $[\text{M}-\text{H}]^-$, 140 - ethanolamine phosphate ion. **c**, Snapshot from MD simulations of neuronal membrane showing reorientation and migration of HpETE-PE peroxidized acyl chain after 50 ns simulation (see Extended Data Fig. 2 for details). **d**, Simulation system (*side view:left and top view:right*) contained lipid bilayer and $\text{iPLA}_2\beta$. ANK fragments are anchored to membrane surface. Cys651 makes close contacts ($< 5.0 \text{ \AA}$) with 15-HpETE-PE molecules (in *cyan space-filling* representation, oxygens in *red*). Each monomer's catalytic dyads (S465 and D598) are shown in *red*. **e**, Intact structural model for $\text{iPLA}_2\beta$ dimer CAT domains with ANK repeats bound to lipid bilayer. **f** $\text{iPLA}_2\beta$ monomers A (*red*) and B (*blue*) with catalytic dyad in *magenta* and R747W in *orange (top)*. Two PLs closely interact with $\text{iPLA}_2\beta$: 15-HpETE with K566-P567 on chain A and SDPE with R656-P657 on chain B. Note that $\text{iPLA}_2\beta$ residues are inserted into the membrane and phospholipids protrude to allow tight ($>3.5 \text{ \AA}$ atom-atom) associations. **g**, $\text{iPLA}_2\beta$ activity in H109 and $\text{fPD}^{\text{R747W}}$ cells. Cell supernatants were incubated with 1-SA-2-ETE-PE (left panel) or 1-SA-2-15-HpETE-PE (*right panel*) for 30 min at 37°C . Activity is presented as (S)-BEL sensitive accumulation of 1-SA-2-OH-PE, pmol/min/mg protein. Data are means \pm s.d., * $p=0.0399$, *** $p=0.0003$, $N=3$ biologically independent experiments, unpaired two-tailed *t*-test. **h**, $\text{iPLA}_2\beta$ protein expression in H109 and $\text{fPD}^{\text{R747W}}$ cells. *Insert*: Representative western blot of $\text{iPLA}_2\beta$. Data are means \pm s.d., $N=3$ biologically independent experiments.

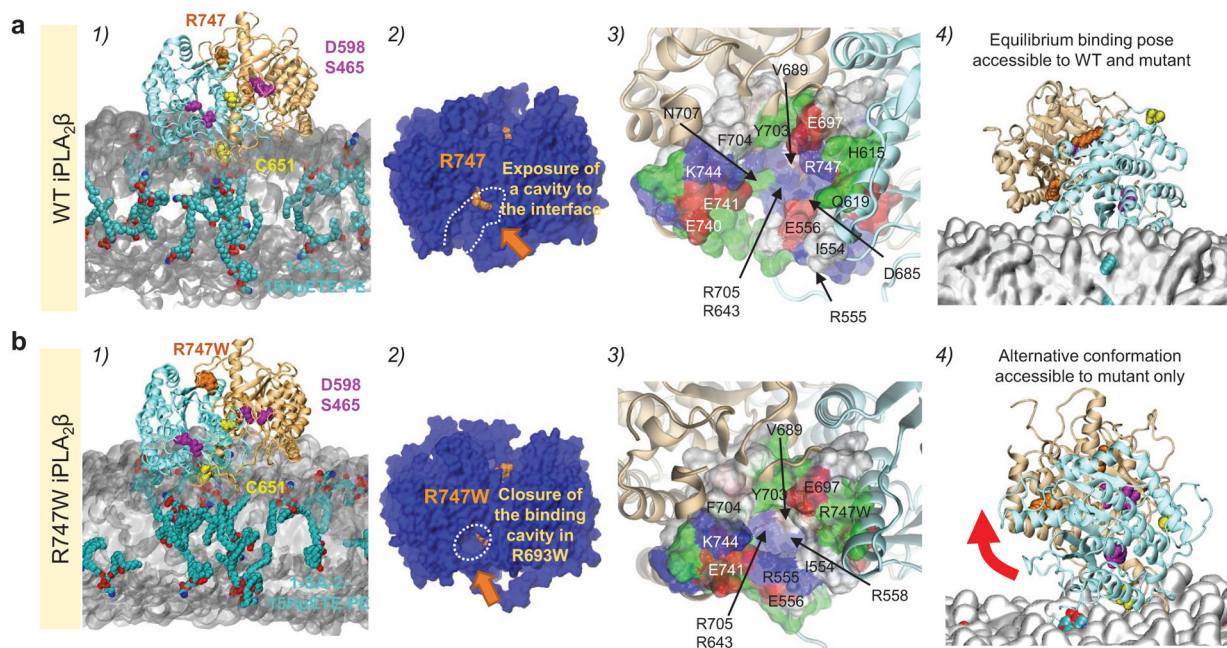


Fig. 2. Computational modeling of the interaction of the iPLA₂β dimer with membrane embedded phospholipids.

Comparison of structure and interactions of WT iPLA₂β (**a**) and R747W mutant (**b**).

Equilibrated structures are comparable (**a-b** panels 1). Major change occurs in an interfacial cavity that closes down in the mutant (encircled by *dashed white shapes* in panels 2), thus restricting access to catalytic site. A closeup view of this region is shown in panels 3. An alternative conformation by the mutant occurs resulting in weaker contacts with lipid membrane (**a-b** panels 4). Residue numbers refer to short-variant (PDB id: 6aun¹⁵) except for R747 (R693 in short variant) which refers to the gene *PNPLA9* numbering.

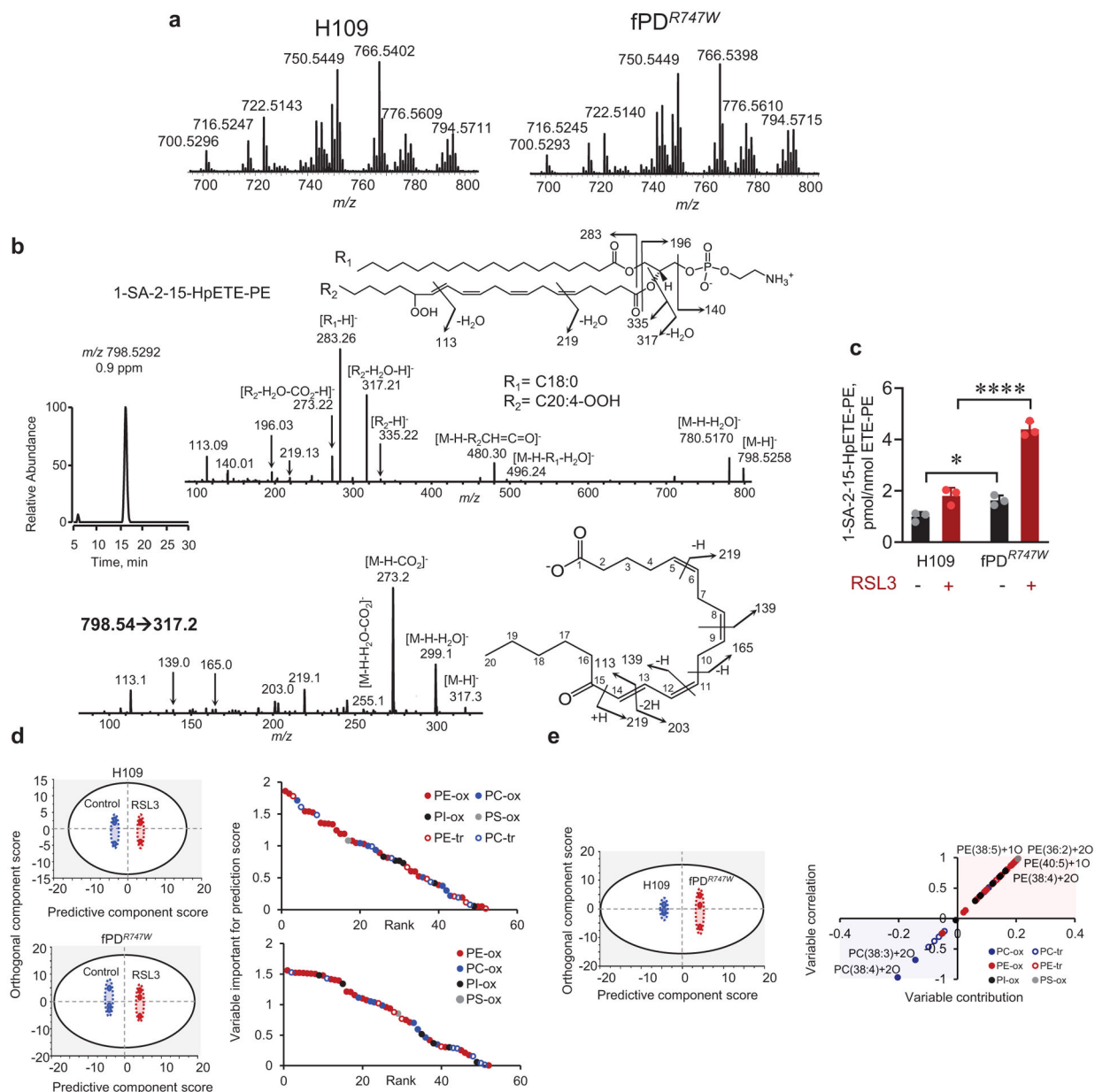


Fig. 3. Lipidomics of H109 and fPD^{R747W} cells.

a, Typical mass spectra of PE from H109 (upper panel) and fPD^{R747W} (lower panel) cells. **b**, LC-MS identification of hydroperoxy-PE species (1-SA-2-15-HpETE-PE) in RSL3 treated fPD^{R747W} cells. Base peak chromatogram (left), MS² (upper right) and MS³ (lower right) spectra of 1-SA-2-15-HpETE-PE (*m/z* 798.5292). Upper inset: structural formula of 1-SA-2-15-HpETE and fragments. Lower Inset: structural formula of molecular ion with *m/z* 317.3 and fragments. Fragments with *m/z* 273 formed by loss of CO₂ from the carboxylate anion; *m/z* 299 originating from the carboxylate anion after loss of water molecule; *m/z* 255 produced after loss of water molecule and CO₂; two *m/z* 219 fragments are generated via C₁₄-C₁₅ bond and C₅-C₆ double bond cleavages, two *m/z* 139 are formed after cleavages of C₈-C₉ and C₁₀-C₁₁ double bonds, respectively, *m/z* 165 generated via C₁₀-C₁₁ bond

cleavage, m/z 203 and m/z 113 produced after C_{13} - C_{14} double bond cleavage, the later one is indicative of the C_{15} position of the ketone group formed after loss of water molecule from 15-HpETE. **c**, Content of 1-SA-2-15-HpETE-PE in RSL3 treated H109 and fPD^{R747W} cells. Cells were exposed to RSL3 (25nM) for 14 hrs. Data are means \pm s.d., * $p=0.0320$, *** $p<0.0001$ vs WT, N=3 biologically independent experiments, two-way ANOVA (Sidak post-hoc test). **d**, Changes in oxidized phospholipidome between control and RSL3 treatment in WT H109 and mutant fPD^{R747W} human fibroblasts. Score plot of OPLS-DA analysis shows the separation of control and RSL3 treated wild type (upper left) and mutant (lower left) fibroblast cells by the oxidized phospholipidome. Dot plot demonstrates variable importance for prediction score of various oxidized PL species in distinguishing control vs RSL3 treatment in WT H109 (upper right) and fPD^{R747W} (lower right) fibroblasts. PEox species are the predominant oxidized species that separate the control from RSL3 treatment. 71% and 70% of the top PLox species that differ significantly between control and RSL3 treatment (variable importance for prediction score >1) are PE-ox species in WT and mutant cells, respectively. **e**, Mutant fPD^{R747W} fibroblasts accumulate greater amounts of PEox species than WT H109 cells upon RSL3 treatment. Score plots of OPLS-DA analysis show differences in oxidized phospholipidome (left). S-plot of OPLS-DA analysis shows variable correlation vs variable contribution for the OPLS-DA model (right). Positive correlation implies accumulation in fPD^{R747W} cells and negative correlation implies accumulation in H109 cells. 80% (12 out of 15) of the top lipids that accumulated in fPD^{R747W} cells (variable correlation >0.8) are PE-ox species whereas higher levels of two PC-ox species were found in H109 cells.

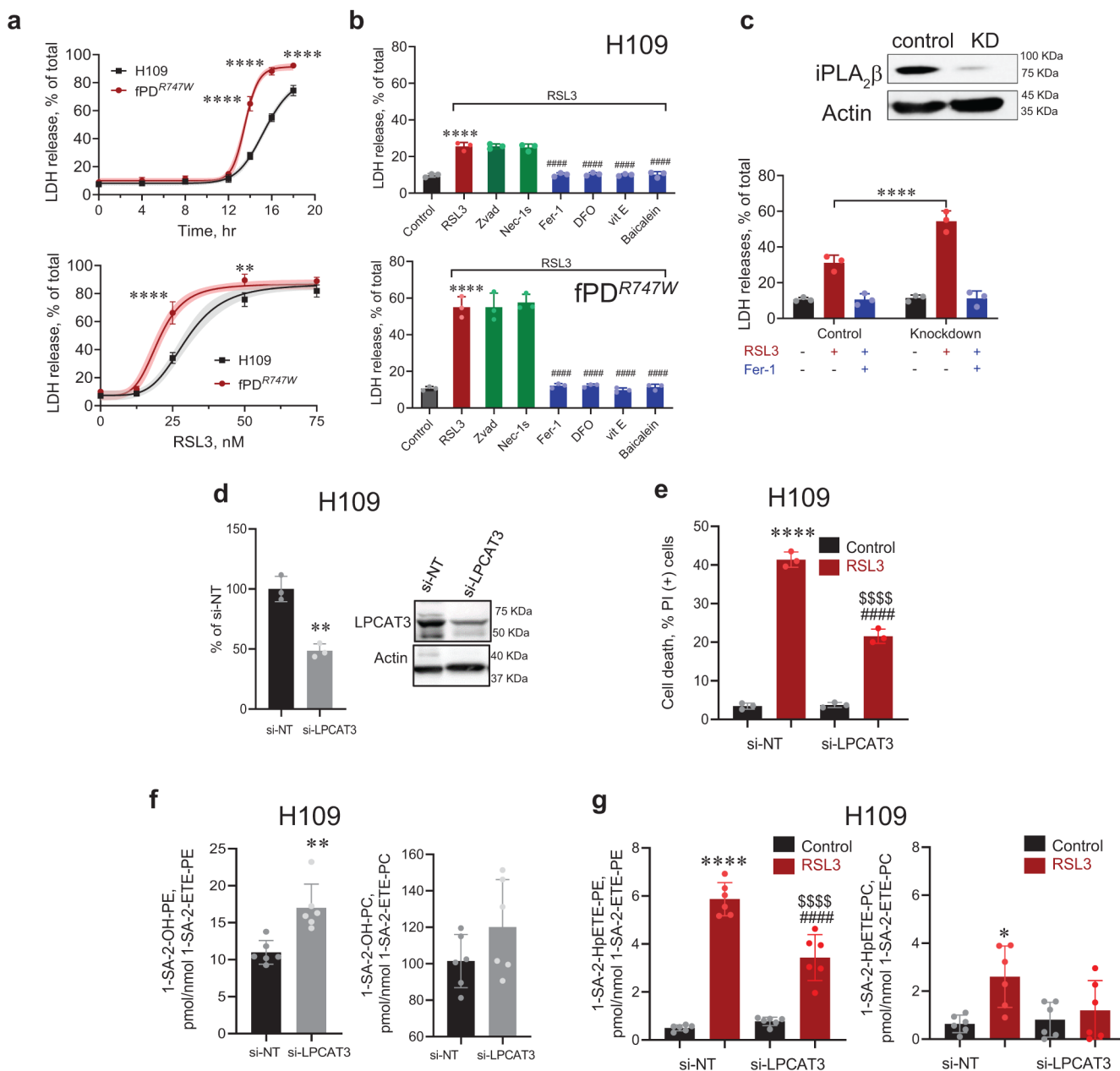


Fig. 4. iPLA₂β-deficient cells are sensitive to RSL3-induced ferroptosis.

a, Time course of RSL3-induced ferroptosis (*upper*) and concentration-dependent effect of RSL3 (*lower*) in WT H109 and fPD^{R747W} cells. Data are means±s.d., **p=0.0018, ****p<0.0001 vs H109, N=3 biologically independent experiments, two-way ANOVA (Sidak's post-hoc test). IC₅₀ was 28.9nM and 22.0nM for H109 and fPD^{R747W}, respectively. **b**, Effect of inhibitors (z-VAD-fmk 50μM, Nec-1s 20μM, Fer-1 0.4μM, DFO 10μM, vit E 10μM, baicalein 2μM) on RSL3-induced (25nM, 14 hrs) death in H109 (*upper*) and fPD^{R747W} (*lower*) cells. Data are means±s.d., ****p<0.001 vs Control, #####p<0.001 vs RSL3, N=3 biologically independent experiments, one-way ANOVA (Dunnett post-hoc test). **c**, RSL3-induced ferroptosis in WT and iPLA₂β knock-down (KD) H109 cells. Cell

death was quantified by LDH release. Data are means \pm s.d., **** $p < 0.001$ vs WT, N=3 biologically independent experiments, one-way ANOVA, (Sidak's post-hoc test). **d, e**, LPCAT3 KD protects H109 cells from RSL3-induced death. **d**, Representative immunoblot and protein levels of LPCAT3 (quantified from three biological replicates normalized to actin). Data represent mean \pm s.d., * $p = 0.0018$ vs si-NT, unpaired two-tailed t -test. **e**, si-NT or LPCAT3 KD cells were exposed to RSL3 (100 nM) and cell death was monitored after 20 hrs by PI staining using flow cytometry. Data are mean \pm s.d., N=3 biologically independent experiments; **** $p < 0.0001$ vs si-NT control, #### $p < 0.0001$ vs si-LPCAT3 control, \$\$\$ $p < 0.0001$ vs si-NT/RSL3, one-way ANOVA (Tukey's post-hoc test). **f**, Quantitative LC/MS-based assessments of lyso-PE (1-SA-2-OH-PE, *left*) and lyso-PC (1-SA-2OH-PC, *right*) in H109 cells. Data are mean \pm s.d., N=6 biologically independent experiments, ** $p = 0.0018$ vs si-NT, unpaired two-tailed t -test. **g**, The contents of oxygenated PE (1-SA-2-HpETE-PE, *left*) and PC (1-SA-2-HpETE-PC, *right*) in H109 cells. Cells were exposed to RSL3 (100nM) for 20 hrs. Data are mean \pm s.d., N=6 biologically independent experiments, * $p = 0.0118$ vs si-NT control, **** $p < 0.0001$ vs si-NT control, #### $p < 0.0001$ vs si-LPCAT3 control, \$\$\$ $p < 0.0001$ vs si-NT/RSL3, one-way ANOVA.

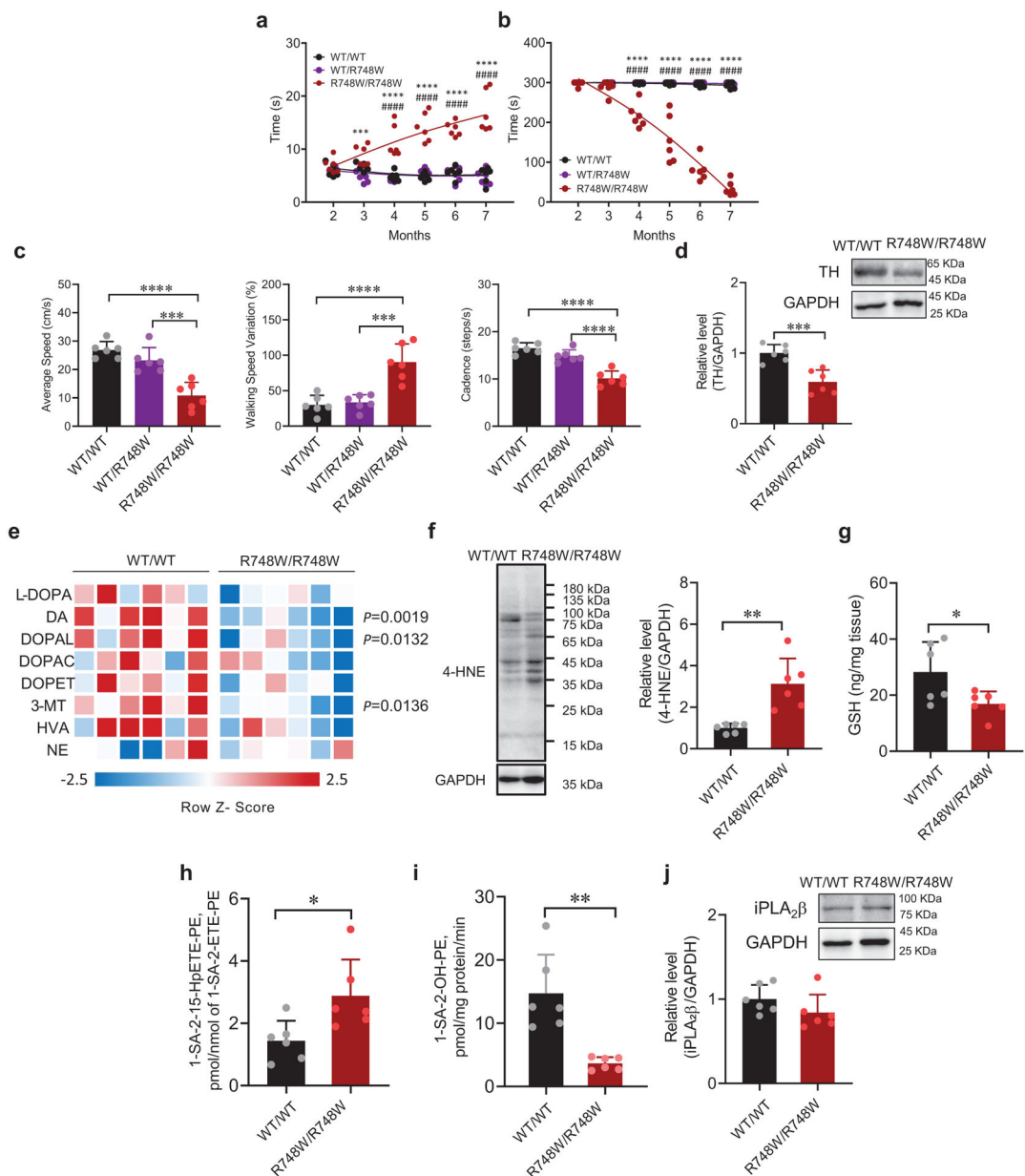


Fig. 5. Homozygous *Pnpla9*^{R748W} leads to Parkinsonian phenotype and ferroptotic oxygenated PE accumulation in midbrain of mice.

a, Time (sec) taken to climb down the pole, and **b**, time (sec) on the rotarod for WT and *Pnpla9*^{R748W} mutant mice at 2–7 months of age. #####*p*<0.0001 vs *Pnpla9*^{WT/WT}, ****p*=0.001 vs *Pnpla9*^{WT/R748W}, *****p*<0.0001 *Pnpla9*^{WT/R748W} N=6 biologically independent animals, two-way ANOVA (Tukey's post-hoc test). **c**, Average walking speed (*left*), walking speed variation (*middle*), and cadence (*right*) of WT and *Pnpla9*^{R748W} mutant mice at 7 months of age in the catwalk test. ****p*=0.0003 for average speed, ****p*=0.0002 for walking speed variations, *****p*<0.0001, N=6 biologically independent animals, two-way ANOVA (Tukey's post-hoc test). **d**, Tyrosine hydroxylase (TH) expression in midbrain of WT and *Pnpla9*^{R748W/R748W} mice. Inset: Representative immunoblot. Data are means ±s.d., ****p*=0.0007, N=5 biologically independent animals, unpaired two-tailed *t*-test. **e**,

Heat map of dopamine and its metabolites in striatum of WT and *Pnpla9^{R748W/R748W}* mice, unpaired two-tailed *t*-test. **f**, Representative immunoblot (*left*) and quantitative analysis (*right*) of 4-HNE expression, and **g** Glutathione (GSH) levels in midbrain of WT and *Pnpla9^{R748W/R748W}* mice. Data are means±SD, ***p*=0.0019, **p*=0.037, N=5 biologically independent animals, unpaired two-tailed student's *t*-test. **h**, 1-SA-2-15-HpETE-PE (known pro-ferroptotic signals) and **i**, iPLA₂β activity in midbrain of WT and *Pnpla9^{R748W/R748W}* mice. 1-SA-2-15-HpETE-PE was used as a substrate. **j**, Representative immunoblot (*top*) and quantitative analysis (*bottom*) of iPLA₂β protein expression; Data are means±s.d., **p*=0.0241, ***p*=0.0014, N= biologically independent animals 5 for iPLA₂β protein expression studies and 6 for all others, unpaired two-tailed student's *t*-test.

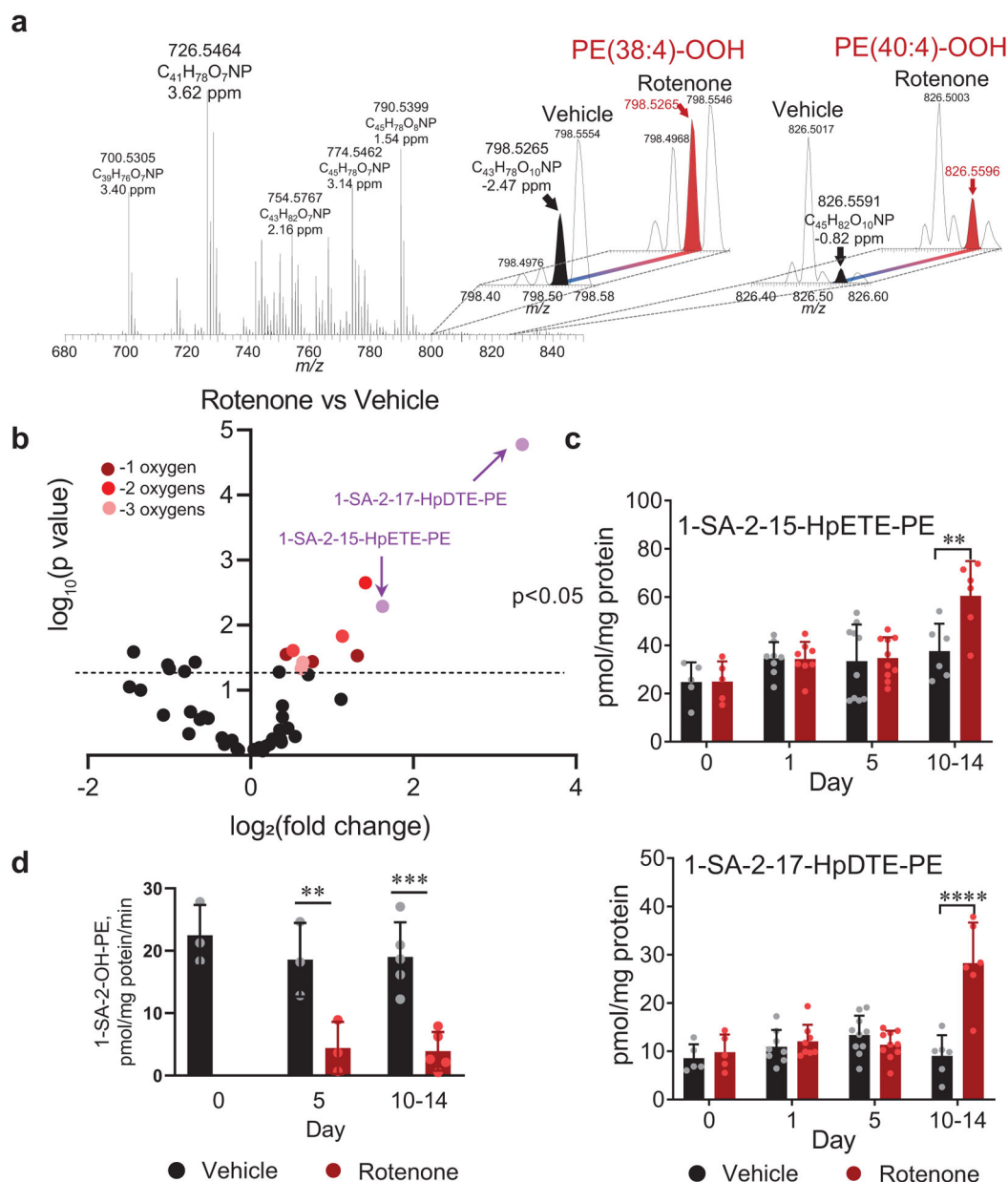


Fig. 6. Accumulation of ferroptotic cell death signals in substantia nigra of rats exposed to rotenone.

a, Typical mass spectrum of PE obtained from *substantia nigra* of rats on days 10–14 after exposure to rotenone. Inset: Mass spectrum of PE in the range of m/z from 798.40 to 798.58 (left) and in the range of m/z from 826.40 to 826.60 (right). **b**, Volcano plots of rotenone-induced changes in the levels of oxygenated PEs [\log_2 (fold change)] vs significance [$-\log_{10}(P\text{-value})$] by t -test in *substantia nigra* of rats exposed to vehicle vs rotenone (ip, 3 mg/kg/day) at Parkinsonian endpoint (Day 10–14). Dark red, red and light red circles represent oxygenated PE with 1, 2, and 3 oxygens added, respectively. Two-tailed student's t -test, $N=6$ biologically independent animals. **c**, Quantitative assessments of 1-SA-2-15-HpETE-PE and 1-SA-2-17-HpDTE-PE (known pro-ferroptotic signals) in *substantia nigra* of vehicle and rotenone-treated rats. Data are means \pm s.d., ** $p=0.0019$, **** $p<0.0001$, $N=5$

biologically independent animals for 0-Day, 6 biologically independent animals for 10–14 days, 8 *substantia nigra* hemispheres from 4 biologically independent animals for Day 1, 10 *substantia nigra* hemispheres from 5 biologically independent animals for day 5, two-way ANOVA (Sidak post-hoc test). **d**, iPLA₂β activity in *substantia nigra* of vehicle and rotenone-treated rats. 15-HpETE-PE was used as a substrate. Data are means±s.d., **p=0.0062, ***p=0.00015, N=3 biologically independent animals for Day 0, Day 5 and 5 biologically independent animals for day 10–14, two-way ANOVA (Sidak post-hoc test).